Simultaneous velocity and density measurements of fully developed Rayleigh-Taylor mixing

Mark Mikhaeil ⓘ,* Prasoon Suchandra ⓘ,* and Devesh Ranjan†
George W. Woodruff School of Mechanical Engineering, Georgia Institute of Technology, 801 Ferst Drive, Atlanta, Georgia 30332, USA

Gokul Pathikonda ⓘ
School for Engineering of Matter, Transport, and Energy, Arizona State University, 551 East Tyler Mall, Tempe, Arizona 85281, USA

The dynamics of molecular mixing and the energy transfer process in the Rayleigh-Taylor instability (RTI) are studied through the collection of simultaneous density-velocity measurements. These experiments provide simultaneous density-velocity field measurements, in contrast to previous point measurements. Statistically stationary experiments are performed in a "convective-type" gas tunnel facility, with density contrast achieved through the injection of helium into the bottom stream. Three experiments at Atwood number ≈ 0.1 are captured at three outer scale Reynolds numbers Re = 520, 2260, and 4050. Particle image velocimetry and laser induced fluorescence are employed simultaneously. Statistics of the density and velocity show self-similar collapse of RTI profiles at large Reynolds number Re > 2000. Flat velocity profiles indicate homogeneous turbulence characteristics in the core of the mixing region. Significant anisotropy develops in the flow, with horizontal velocity fluctuations being only 60% of the vertical velocity fluctuations. The turbulent mass flux is found to be asymmetric about the centerline, with increased peak towards the spike. Measurements of the molecular mixing show that mixing is maximized at the core of the flow and increases with increased Reynolds number. The transport equation of density-specific-volume correlation b shows that it is mostly produced in the core of the mixing region, and that the spatial evolution of its profile is the result of transport by bulk motion of the bubble and spike. Energy transfer from gravitational potential energy to turbulent kinetic energy and viscous dissipation is observed to occur in the experiment with a ratio of dissipated energy to potential energy released of 38%. The analysis of the turbulent kinetic energy transport equation budget reveals that production is the primary mechanism towards the growth of turbulent kinetic energy in the core of the flow, and is asymmetrically slightly skewed towards the spike. However, it is through the transport that the strong advection at the edges of the mixing region is maintained.

I. INTRODUCTION

Rayleigh-Taylor instability (RTI) driven turbulent mixing occurs in a variety of phenomena extending an enormous range of length scales. At astronomical scales, RTI mixing is an important mechanism in the understanding of type Ia supernovas [1–5]. At micron scales, RTI hydrodynamics

---

*These authors contributed equally to the work.
†devesh.ranjan@me.gatech.edu

play an integral part in the physics of inertial confinement fusion [6–11]. Between these two examples of RTI turbulent mixing at extreme conditions exist many other natural and synthetic situations including spray atomization [12], premixed combustion [13], salt dome formation [14], estuary flow [15], and atmospheric and oceanic convection [16]. In all of these scenarios, the difference in density between fluids in a gravitational or acceleration field leads to perturbation growth, and the fundamental understanding of RTI is crucial to the development of theories and predictive models.

The Rayleigh-Taylor instability occurs at the unstable perturbed interface between two fluids of different densities. If the gradients of pressure and density are misaligned such that $\nabla p \cdot \nabla \rho < 0$, then baroclinic vorticity deposition causes the interface to roll up in such a way as to grow the perturbation. In many applications, the pressure gradient is caused by hydrostatic forces, governed by the gravitational acceleration g. The density gradient is caused by differences in densities between the heavy fluid with density ρ_1 and the light fluid with density ρ_2. The difference between the densities is nondimensionalized by the Atwood number $\mathcal{A}$ defined by Eq. (1):

$$\mathcal{A} = \frac{\rho_1 - \rho_2}{\rho_1 + \rho_2}. \tag{1}$$

At small values of $\mathcal{A}$, the flow may be analyzed using a Boussinesq approximation [17], as the variation of density is considered to have negligible impact on the inertial properties of the fluid, and only serves to cause buoyant forces. As $\mathcal{A}$ exceeds approximately 0.2, the Boussinesq approximation becomes invalid and variable-density effects have significant importance in the inertial properties of the fluid and subsequently on the production of turbulence.

The growth of RTI falls into various stages [18]. Typical RTI structures take on the appearance of alternating and interpenetrating *bubbles* of rising light fluid and *spikes* of falling heavy fluid. If $\mathcal{A} \approx 0$, the bubble and spike structures are largely symmetric, but as $\mathcal{A} \to 1$ asymmetry develops between the bubble and the spike leading to wide, round bubbles separated by narrow, sharp spikes. In the final stages of RTI, various mechanisms cause the breakup of the bubble and spike structures and the development of a large range of scales characterized by small-scale vortices. Thus, the flow field enters a fully turbulent state. Here, the flow is thought to become self-similar and lose memory of its initial perturbation so that the only physical scale remaining is the half width of the mixing region, h [19]. Early experiments in this fully turbulent regime by [20] found that h grew quadratically in time elapsed from the onset of instability, also called the instability development time t by Eq. (2):

$$|h_{b,s}| = \alpha_{b,s} \mathcal{A} g t^2 \tag{2}$$

where $h = (|h_b| + |h_s|)/2$ with $|h_b|$ being the magnitude of the bubble height and $|h_s|$ being the magnitude of the spike height. This quadratic growth rate has been confirmed through a variety of methods, like the extension of the linear theory [21], dimensional analysis [22,23], self-similarity applied to the Navier-Stokes equations [19], experiments [20,24–28], and simulations [29–31]. In Eq. (2), α_b is the bubble growth rate parameter and α_s is the spike growth rate parameter. The half width of the mixing region h can also be written as $h = \alpha \mathcal{A} g t^2$ where α is the averaged RTI growth rate parameter. Experiments and simulations have shown that this parameter can take on a wide range of values from 0.02 to 0.16, depending on the density ratio, acceleration, and initial perturbation [32]. Numerical simulations report values of α_b closer to 0.02 as they are mostly initialized with small wavelength, a white noise type of initial perturbations, while experiments have long wavelengths and produce mixing regions that have α_b which are historically larger (0.05–0.08) [32–34]. Furthermore, as $\mathcal{A} \to 1$, structural asymmetry develops between the bubble and the spike, causing the bubble growth rate parameter α_b to differ significantly from the spike growth rate parameter α_s.

The precise point of mixing transition to the fully turbulent regime is an unanswered question. Dimotakis [35] notes that jet flows exhibit a qualitative transition in phenomenology as their outer scale Reynolds number exceeds a critical value, $\mathrm{Re}_{\mathrm{tr}} \approx 1$–$2 \times 10^4$, or as the Taylor-Reynolds

number exceeds a critical value, $\mathrm{Re}_{\lambda,\mathrm{tr}} \approx 100$. He generalizes this concept into a hypothesis that other flows also transition to turbulence at a similar Reynolds number. In the case of RTI, the outer scale Reynolds number is most often defined by Eq. (3):

$$\mathrm{Re} = \frac{UL}{\nu} \tag{3}$$

where ν is the kinematic viscosity of the mixture. For RTI flows, L is typically chosen to be some multiple of the mixing half width, h. U is typically based either on the growth rate of the mixing width, $\dot{h} = \frac{\partial h}{\partial t}$, or on some measure of the velocity of the turbulence, such as the root-mean-square velocity fluctuations, v'_{rms}. Nevertheless, neither the transition criteria presented by [35] nor the appropriate length or velocity scale for the Reynolds number are universally recognized, and the precise dynamics and structure of the fully turbulent regime is still a point of contention.

Studying the RTI fully turbulent regime using transient experiments [28,36–38] requires a prohibitively expensive amount of experimental time. To overcome this limitation, [39] designed a "convective-type" or *statistically stationary* experimental facility in which two fluids of different densities flowed parallel to one another separated by a thin splitter plate. The streams met each other as they flowed past the splitter plate and into an optically accessible test section, and RTI developed at the unstable interface between the two streams. The instability continued to grow as the fluids convected across the test section and out of the facility. At its core, this facility applied Taylor's hypothesis [40] to transform the instability development time, t, into the streamwise distance from the splitter plate, x, through the convective velocity U_c by $x = U_c t$, similar to the procedure utilized in grid turbulence experiments [41]. Rather than conducting several experimental realizations to compile a statistical ensemble of RTI structures, a probe or camera was placed at a stationary position in the flow and captured hundreds or thousands of instances of fully turbulent structures as they convected past the measurement location.

The first statistically stationary experimental facility built was the water channel facility developed by [39]. It used hot and cold water ($\mathcal{A} \approx 1 \times 10^{-3}$), with one fluid marked with nigrosin dye to capture the first measurements of concentration profiles across the mixing height at different measurement times. They also collected measurements of the growth rate parameter, estimating that $\alpha = 0.07$. Later experiments by [42,43] in the same facility using thermocouple arrays with high temporal resolution allowed the quantification of the power spectrum of density fluctuations, first suggesting the existence of a $-5/3$ power law scaling. The first velocity measurements in the water channel were collected by [44], who used particle image velocimetry (PIV) to capture streamwise and cross-stream velocity fields and statistics. By seeding the top and bottom water streams with different concentrations of PIV particles, an estimate of the stream concentrations could be found, giving a simultaneous density measurement (this was referred to as PIV-scalar). This experiment was improved in [45] and showed that velocity profiles collapsed onto self-similar forms at later development times. They also found the existence of a -3 power law scaling for the dissipation range using data from a high temporal resolution thermocouple array. Later experiments by [46,47] analyzed the modal content of the initial condition and quantified the effect of Schmidt number on the extent of molecular mixing. In this regard, [47] was the first to link RTI back to the fundamental problems of turbulent mixing [35].

To study the RTI fully turbulent regime in the non-Boussinesq regime, [27] developed a gas tunnel facility analogous to the water channel facility which used air and an air-helium mixture as the two fluids. Further modifications to this gas tunnel by [48,49] helped capture simultaneous velocity-density statistics at Atwood numbers up to $\mathcal{A} = 0.6$. Results from the gas tunnel facility showed that the RTI mixing layer at large $\mathcal{A}$ was strongly anisotropic with velocity fluctuations in the acceleration direction, v', being approximately twice as strong as in the acceleration normal directions, u' and w'. They also elaborated on the extent of asymmetry between the bubble and spike structures.

The current state of RTI research is distinguished by high-resolution and high-speed photography, laser imaging techniques, and extensive data sets providing significant statistical information

[50,51]. Reference [34] improved upon the design of the gas tunnel facility used by [27,49], allowing the measurement of RTI turbulent mixing at $\mathcal{A} = 0.73$. By implementing planar PIV, velocity profiles could be computed across the entire mixing region, and showed the same self-similar collapse that had been previously shown by [45]. In addition, velocity statistics across the layer showed the same anisotropy present in the experiments of [49]. Further work by [52,53] showed the impact of overlying shear on the growth of the fully turbulent RTI and determined a criteria based on the Richardson number of the flow in order to determine if the growth was dominated by shear or buoyant forces.

The current paper aims to capture simultaneous density-velocity-field measurements of a statistically stationary Rayleigh-Taylor instability experiment with gases using a combined PIV and laser induced fluorescence (LIF) technique. The details of how the current paper overcomes various diagnostics-related challenges associated with simultaneous PIV and LIF can be found in [54]. Molecular mixing and its evolution are studied. We also dig into the energy transfer process in RTI driven flow. Different terms of the transport equation of turbulent kinetic energy are evaluated using the collected PIV-LIF data and the model based on [55]. These experiments and analyses provide a lot of insight into dynamics and energetics of RTI driven flows which are anisotropic and inhomogeneous in nature. These understandings will help accentuate or control Rayleigh-Taylor instabilities as per requirements of certain engineering applications. The statistics collected and calculated from these experiments are supposed to be useful parameters for researchers trying to numerically model RTI driven flows.

II. METHODS

A. Experimental facility

Experiments are performed in the gas tunnel facility, illustrated in Fig. 1. The base of the facility is that used by [34], but has been modified to capture combined density-velocity statistics using simultaneous PIV-LIF. Two fluid streams, one heavy and one light, flow separately through the tunnel operated by a suction fan. They remain separated until they pass the splitter plate dividing them and enter the test section, where they begin to mix with one another. They continue to mix as they convect across the test section. The major benefit of the gas tunnel facility is that it is statistically stationary—at any location in the flow, time gradients of mean quantities are zero [39]. In this convective-type facility, Taylor's hypothesis [40] is used to transform the development time of the instability, t, to the streamwise location, x, through the convective velocity, U, by $x = Ut$. As a result, higher-order moments, probability density functions (PDFs), structure functions, and spectra can be measured at specific RTI mixing times by recording measurements at a single streamwise location for a long period of time. The origin of the coordinate system is defined as the center of the splitter plate knife edge at the entrance of the test section, as in Fig. 1. The density difference between the two fluid streams is achieved by injecting a "lighter-than-air" gas mixture, consisting
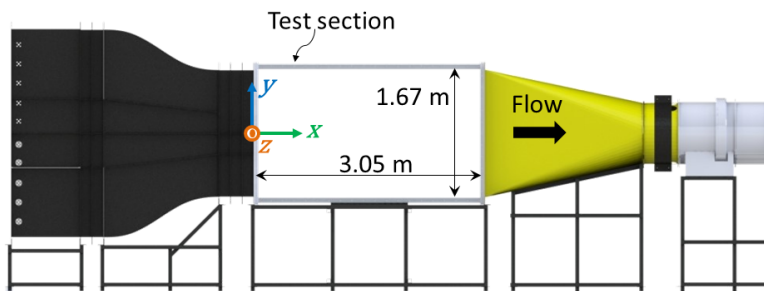

FIG. 1. 3D render of the gas tunnel facility.

of helium, nitrogen, and air, into the bottom stream of the gas tunnel facility. In order to maintain a constant Atwood number during the experiment, it is necessary to precisely control the mass flow rate of the injected fluid. Details of the light gas injection system can be found in [54].

B. Scales for imaging diagnostics

The results of [34] provide first-order estimates of length and time scales present in the flow. The outer scale of the flow, L, is on the order of the half-mixing height, $h = 0.2$ m, and the fluctuating velocity scale is on the order of the total mixing height growth rate. To estimate this, we take the time derivative of the RTI self-similar growth rate, Eq. (2), to find that $\dot{h} = 2\alpha \mathcal{A} g t = \sqrt{4\alpha \mathcal{A} g h}$. With estimates of the growth rate parameter, Atwood number, and gravitational acceleration of $\alpha = 0.06$, $\mathcal{A} = 0.1$, and $g = 9.8\,\mathrm{ms}^{-2}$, respectively, we arrive at an estimate for the growth rate as $\dot{h} = 0.22\,\mathrm{ms}^{-1}$ and the associated Reynolds number of the flow as Re = 5100. Using the dimensional analysis as suggested in [56], we find an estimate of the Kolmogorov microscale in the present facility as $\eta = 0.33$ mm and the Kolmogorov time scale, τ_η, as $\tau_\eta = 6.4$ ms. The experiments presented involve miscible fluids, so we expect that molecular diffusion will have an impact on the fluid mixing. The strength of molecular diffusion is quantified by the Schmidt number Sc $= \nu/D$, where ν is the kinematic viscosity of the fluid and D is the molecular diffusivity. The scale at which molecular diffusion takes place is termed the Batchelor scale, $\eta_B = \eta/\mathrm{Sc}^{1/2}$. The Schmidt number describing the diffusion of helium into air is approximately Sc $= 0.22$, leading to a Batchelor scale in the present flow $\eta_B = 0.70$ mm, larger than the Kolmogorov microscale. Like the Kolmogorov microscale, dimensional arguments [56] can be used to find an estimate for the Taylor microscale λ, in terms of the outer scale and Reynolds number. The estimate of the Taylor microscale in the present facility is $\lambda = 8.85$ mm and $\mathrm{Re}_\lambda = u'\lambda_T/\nu = 113$. The measurement of the Taylor microscale in the flow is useful for the evaluation of transition to turbulence. Therefore, it is vital that our diagnostic imaging techniques have resolution at least as fine as half the Taylor microscale, accounting for the Nyquist sampling criterion.

C. Particle image velocimetry

For PIV seeding, an olive oil based Laskin nozzle aerosol generation system is built (details in [54]) giving suspended particles of median size 1 μm [57], resulting in a Stokes response time of 10 ms [58]. On observation of the particle response time, we find that this timescale is about three orders of magnitude smaller than the predicted Kolmogorov time scale, giving confidence that the particles accurately track the smallest fluctuations in the flow.

The particles are illuminated by a laser sheet generated by diverging the beam of a Litron NanoPIV 532-nm Nd:YAG laser, capable of emitting 110 mJ per pulse. The light sheet is generated as shown in Fig. 2. The light sheet is scattered by the olive oil aerosol and the illumination is acquired by two TSI PowerView 29MP CCD cameras, fitted with Nikon 50-mm $f/1.8$ lenses. To increase the frame rate of the acquisition, the cameras are operated in 2×2 binning mode and 12-bit dynamic range, resulting in a PIV image resolution of 3300×2200 px and a camera frame rate of 1.25 Hz. A Berkley Nucleonics Corp Model 575 delay generator synchronizer controls the timing of the laser and the camera. PIV correlation maps and vectors are calculated using LaVision DaVis 8.4 software (details in [54]).

The final result is an Eulerian description of the x-direction velocity u and y-direction velocity v, in the x-y plane (refer to Fig. 1). The final field of view imaged is approximately 5 cm in x extent and 80 cm in y extent, with a vector spacing of ≈ 1.1 mm/vec.

D. Laser induced fluorescence

To complement the velocity measurements captured by PIV, LIF measurements are captured to analyze the density field. LIF is accomplished by seeding the light gas with acetone vapor, which fluoresces under excitation by 266-nm light. The details of the acetone bubbler design and its working can be found in [54].
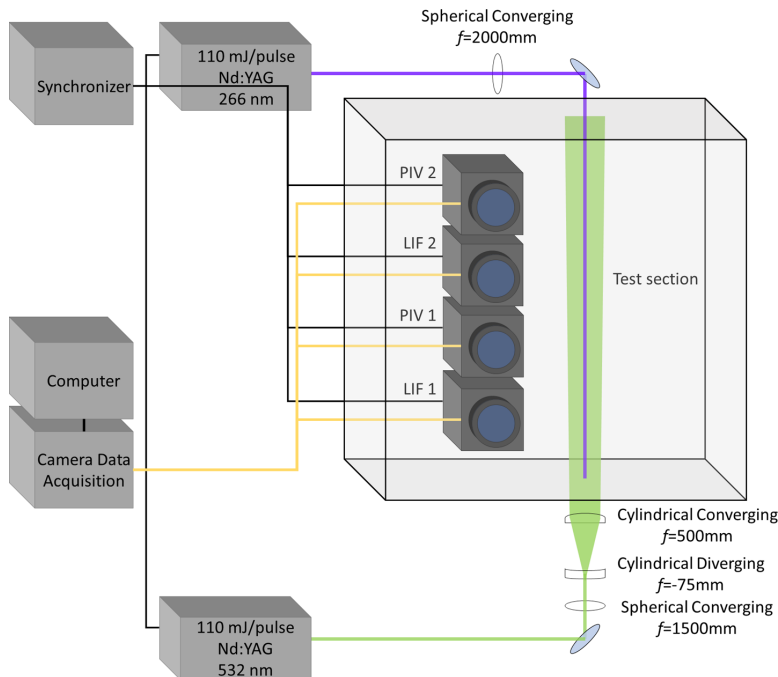
FIG. 2. A simplified schematic showing the PIV and LIF laser, optics, and camera setups.

A Litron laser model capable of producing 110 mJ per pulse at 266-nm wavelength is used as the energy source for LIF. The emitted beam is focused by the use of a 2000-mm focal length converging spherical lens and oriented in the test section vertically, as shown in Fig. 2.

Similar to the PIV setup, two TSI PowerView 29MP CCD cameras with Nikon 50-mm $f/1.2$ lenses are used to capture the fluorescence signal. To prevent the scattering from PIV particles from appearing in the image, a 532-nm wavelength notch filter is added to the lenses. To maximize the signal response and frame rate, the cameras are operated in 8×8 px binning mode and with 14-bit resolution. This allows data to be captured at a rate of 1.25 Hz. In order to ensure that the LIF fluorescence and the PIV scattering do not appear in the same images, the LIF laser pulse is fired 200 ms before the first PIV laser pulse.

The images captured need to be corrected in order to extract the quantitative concentrations of the heavy and light gas, f_1 and f_2, respectively, across the y axis. When coupled with the density information of the incoming streams, these concentrations can be used to determine the density field, ρ. The steps taken in processing the LIF raw images are illustrated consecutively in Figs. 3 and 4 (more details in [54]). The final result is a LIF data table of x, y, and f_2 measurements along the path length of the beam. The overall field of view captured by the LIF cameras is a narrow line approximately 80 cm in y extent, with a resolution of ≈ 0.28 mm/px. The concentrations along the beam path have been filtered by a Gaussian filter with half width ≈ 1 mm, which corresponds to ≈ 4 px.

The primary achievement of the combined PIV-LIF technique is the simultaneous measurement of density and velocity, and therefore the ability to describe how the dynamics and mixing in the RTI flow are linked.

III. RESULTS

At small $\mathcal{A} \approx 0.01$, the sensitivity of the gas stream densities to small variations in temperature can lead to large uncertainties in the experimental Atwood number. At large $\mathcal{A} \approx 0.7$, the large
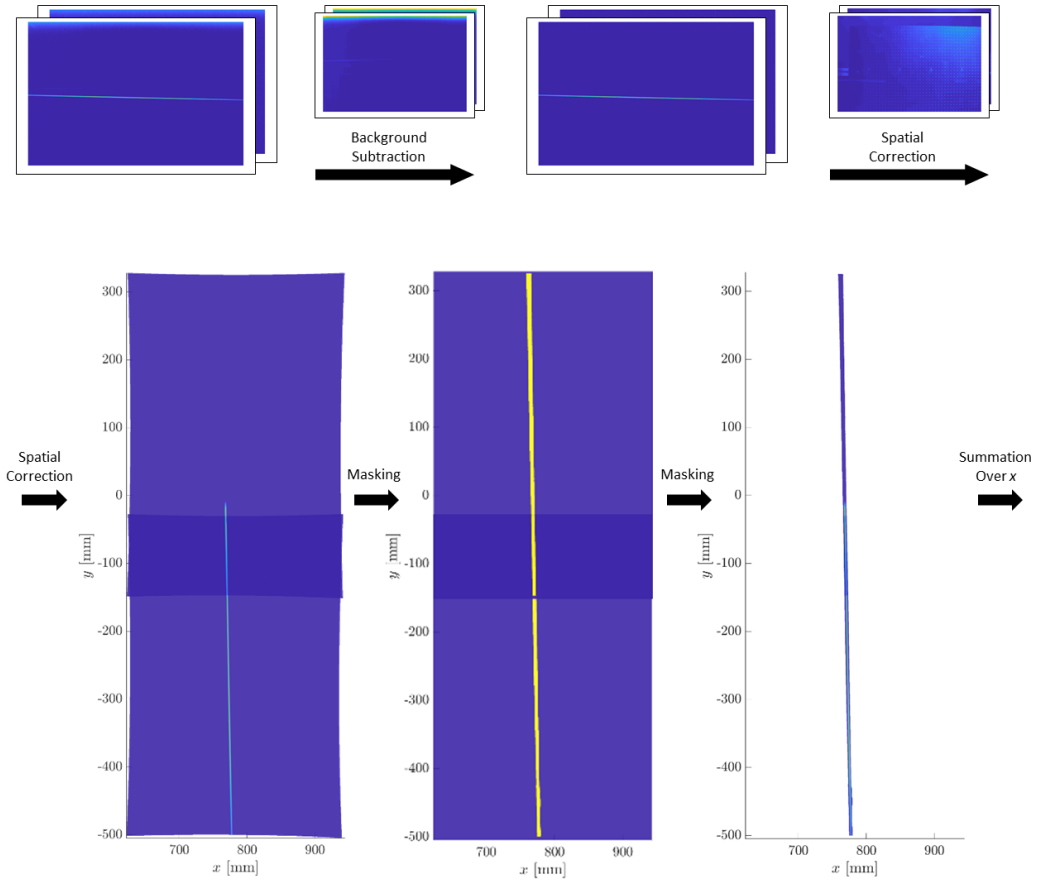
FIG. 3. Methodology for processing the LIF images (part a).

injection flow rates lead to fast depletion of helium storage tanks, resulting in short and insufficient time to acquire large experimental data sets. Thus $\mathcal{A} = 0.1$ is selected as an appropriate Atwood number for these experiments. The convective velocity is selected so that the total mixing width would reach approximately half the total height of the tunnel, by the time the flow reaches $x = 1.75$ m. This allows the flow at this location to remain encapsulated within the field of view of the diagnostics, and to avoid undesirable effects at the end of the test section [54]. The convective velocity of the tunnel is set to $U_c \approx 1.45 \, \mathrm{ms}^{-1}$.

As the flow convects through the tunnel and the mixing height grows, the Reynolds number based on mixing height increases. Many previous RTI experiments, such as [34,45], show that a transition to a self-similar state occurs at Re > 1000. Therefore, two Reynolds numbers past this state are selected in order to test if self-similarity was achieved. In addition, one Reynolds number below this criteria is selected to point out differences between the flow conditions before and after the transition to self-similarity. All together, three Reynolds numbers are chosen for these experiments, Re $\sim$ 500, 2000, and 4000, which occur, respectively, in the flow at downstream locations of $x \sim$ 0.75, 1.25, and 1.75 m.

Table I lists the settings for the three experiments conducted. The Reynolds number is based on the mixing height found from LIF data and the fluctuating velocity components found from PIV. The gas densities and Atwood numbers are found from the pressure and temperature measurement devices equipped on the light gas injection line and in the gas tunnel streams. These densities and the associated fluid concentrations are used to compute the gas mixture viscosity, using the
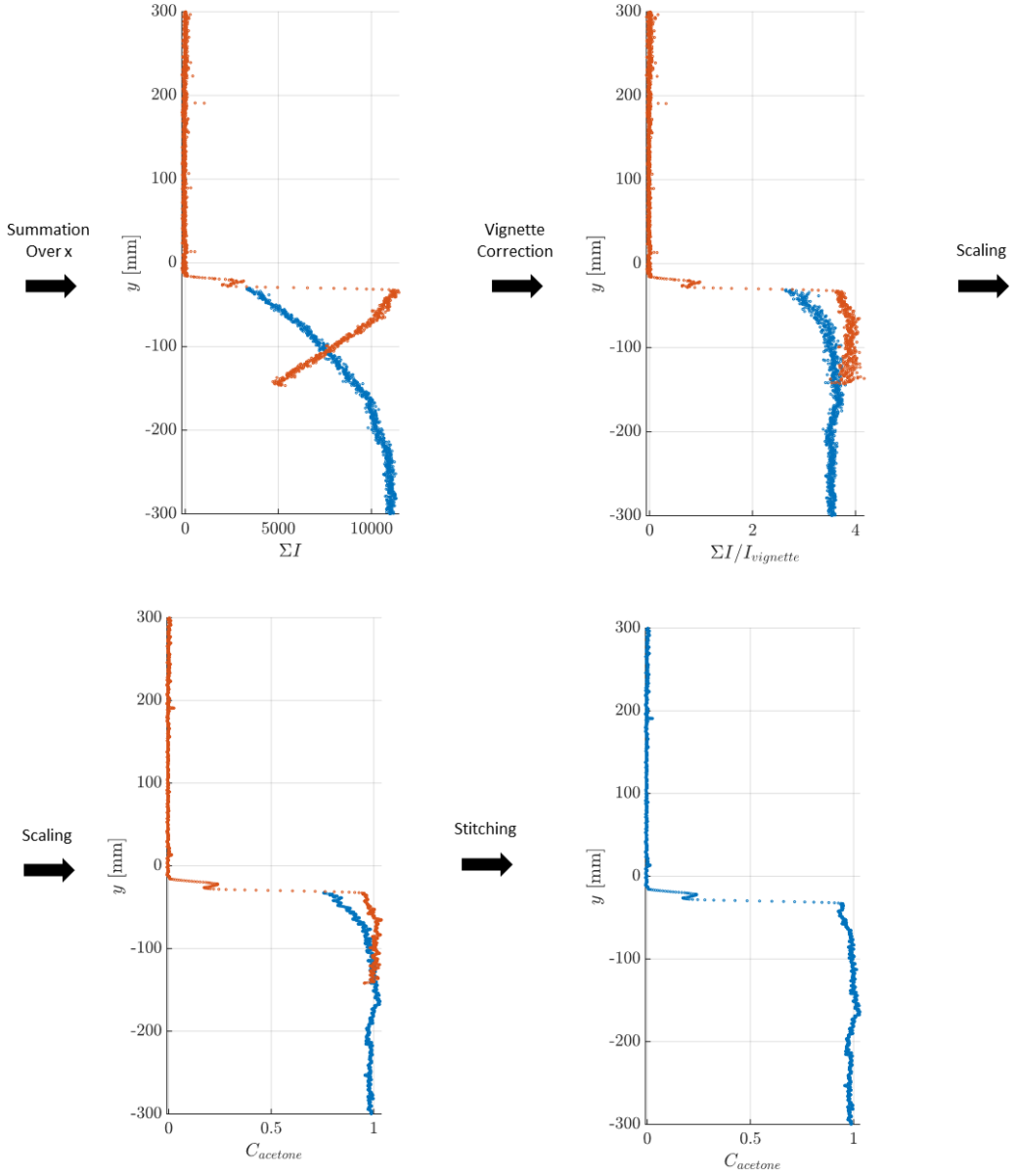
FIG. 4. Methodology for processing the LIF images (part b).

TABLE I. Outline of experimental settings for the simultaneous PIV-LIF campaign.

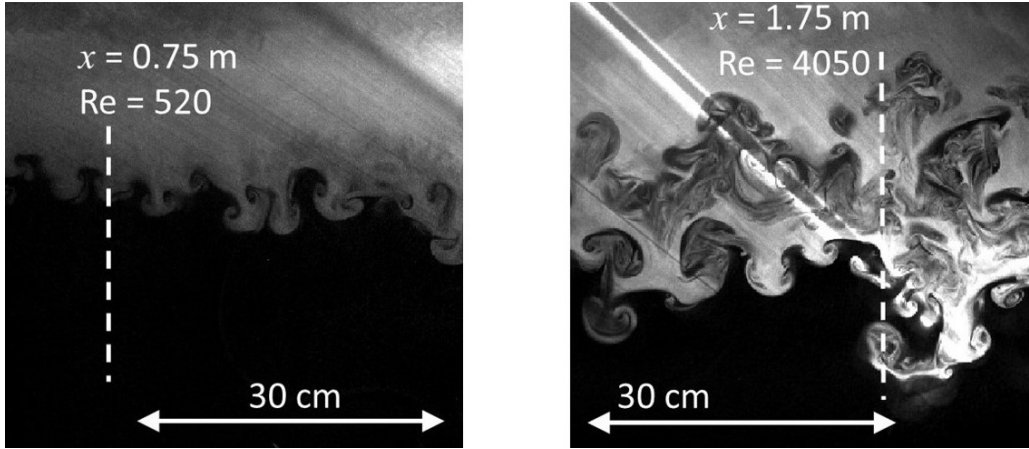| Re	x (m)	$\mathcal{A}$	ρ_1 (kgm^{-3})	ρ_2 (kgm^{-3})	U_c (ms^{-1})	ν (m^{2}s^{-1})
520	0.75	0.098	1.176	0.966	1.42	1.687×10^{-5}
2260	1.25	0.092	1.171	0.973	1.53	1.677×10^{-5}
4050	1.75	0.096	1.167	0.963	1.48	1.684×10^{-5}

FIG. 5. Mie-scattered instantaneous images of the RTI mixing region. The vertical dashed white line indicates the position of the streamwise distance x and corresponding Re. The horizontal white line indicates a length scale of 30 cm.

method of [59]. The convective velocities are found from PIV, and used to compute the instability development time by applying Taylor's hypothesis, together with the streamwise location. The total usable experimental time for each experimental location is approximately 220 s, and at the 1.25-Hz capture frequency of the PIV-LIF cameras this results in an ensemble of 275 image captures per experiment.

Figure 5 shows two representative Mie-scattered instantaneous images of the RTI mixing region, showing features of bubbles and spikes at two Re. At low Re, the mushroomlike structures of bubbles and spikes remain intact, and there is minimal mixing between the two fluids. As the instability grows and reaches higher Re, complex features start to develop in the flow. As the bubble and spike move past one another, unmixed fluid is entrained in the shear rollups and a greater extent of mixing is observed between the two fluids.

A. LIF results

Processing a single acquired LIF image provides an instantaneous measure of the volumetric concentration of fluorescent acetone marker $C_{acetone}$ at each y location along the path of the excitation laser beam. The density of the flow can then be found with the assumption that the acetone concentration is a perfect marker of the volumetric concentration of the bottom stream. The resulting equation for density, $\rho = \rho_1(1 - C_{acetone}) + \rho_2 C_{acetone}$, is applied to each instantaneous LIF capture to obtain the instantaneous density profile. A measure for the instantaneous volume fraction of fluid 1 (the fluid of larger density), f_1, can then be found as $f_1 = (\rho - \rho_2)/(\rho_1 - \rho_2)$, and the corresponding instantaneous volume fraction of fluid 2, f_2, can be found as $f_2 = 1 - f_1$.

Because the gas tunnel facility is statistically stationary, ensemble averages of instantaneous measurements are equivalent to temporal averages (although at a small temporal resolution of 1.25 Hz). In this paper, we show the ensemble averages of a set of instantaneous measures $\{\phi_1(x, y), \phi_2(x, y), \ldots, \phi_N(x, y)\}$ as $\overline{\phi}(x, y) = \frac{1}{N} \sum_{i=1}^{N} \phi_i(x, y)$. The fluctuating components ϕ_i' are then found by subtracting the ensemble mean from the instantaneous measurement, $\phi_i' = \phi_i - \overline{\phi}$.

Measures for the bubble height, h_b, and spike height, h_s, are found from the profiles of $\overline{f_1}$ by finding the y locations at which $\overline{f_1} = 95$ and 5%, respectively. The centerline of the mixing region, y_0, is then defined as the average between h_b and h_s, $y_0 = (h_b + h_s)/2$, and the half width of the mixing region, h, is defined as half the distance between h_b and h_s, $h = (h_b - h_s)/2$. The values of these measures are presented in Table II.

TABLE II. Measures of the bubble and spike heights, the half width of the mixing region, and the mixing centerline for the three Reynolds numbers investigated.

Re	Spatial widths (cm)				
	h_b	h_s	h	y_0	h_f
520	2.08	−4.82	3.45	−1.37	8.69
2260	11.12	−10.09	10.60	0.51	27.48
4050	16.26	−16.34	16.30	0.04	38.41

Reference [24] outlined another method for calculating the mixing width based on the assumption that the volume fraction f_1 profile is linear through the mixing region and transitions sharply to a constant of unity at the top edge of the mixing region and a constant of zero at the bottom edge. The total mixing height, h_f, can then be found by performing an integral over the domain of the two volume fractions:

$$h_f = 6 \int_{-\infty}^{\infty} \overline{f_1}(1 - \overline{f_1})dy \tag{4}$$

where the factor of 6 comes from the assumption that the RTI concentration profile is linear through the mixing region. h_f can be used to construct a nondimensional spatial parameter, $Y_f = (y - y_0)/h_f$, similar to the way that we previously used the mixing width h to construct Y. The measures of h_f for the three experiments performed are presented as a separate column in Table II, and the profiles of the mean volume fraction normalized against h_f are presented in Fig. 6. Good collapse is shown in the profile shape, and it appears that the linear profile gives a good estimate of the gradients of the volume fraction through the core of the mixing region, only showing deviation from the measured data at the edges of the mixing region.

There is significant research interest in the measurement of the RTI growth rate parameter, α. Most methods for the computation of α, like the virtual origin method [39] or the self-similar growth rate method of [19], require the continuous measurement of h at many instability development times, t. A comparison of different such methods is provided in [49]. We are limited in the current experiment with only three measurements. However, [60] outlines a method for calculating α based on only a few measurements taken in the self-similar regime. If $h(t_1)$ and $h(t_2)$ represent two measurements of h taken at different instability development times in the self-similar regime, then

$$\alpha = \left(\frac{h(t_2)^{1/2} - h(t_1)^{1/2}}{(\mathcal{A}g)^{1/2}(t_2 - t_1)} \right)^2. \tag{5}$$

This equation can be found by integrating the self-similar growth rate equation over time. We can apply this methodology using the results from the two largest Reynolds number experiments to find an estimate of the growth rate parameter and its uncertainty, the value being close to that found in other experimental works [34,37,45]:

$$\alpha = 0.049 \pm 0.009. \tag{6}$$

Using the bubble height h_b instead of the half width of the mixing region h in Eq. (5) gives $\alpha_b = 0.039$.

Finally, Fig. 7 shows the root-mean-square fluctuations of the density for the three Reynolds numbers tested. Interestingly, while the density fluctuations remain at a similar value at the edges of the mixing layer, there is a trend towards smaller core fluctuation values as the Reynolds number increases. This suggests that as the flow develops and molecular mixing begins to occur the inhomogeneity of material in the core of the mixing region decreases.
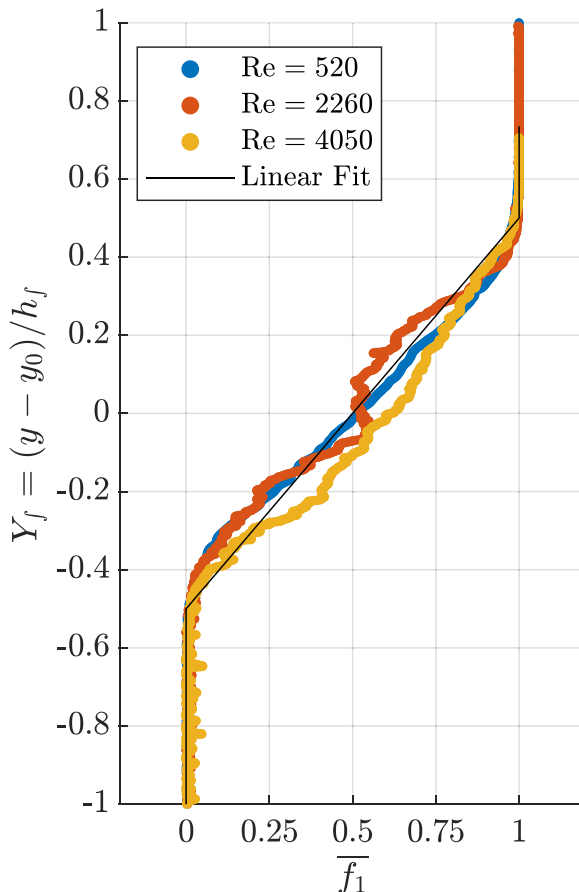
FIG. 6. Normalized profiles of the mean volume fraction of the heavy gas $\overline{f_1}$ for the three Reynolds numbers tested, but with the spatial coordinate normalized by h_f instead of h. Superimposed is the linear volume fraction profile assumed by [24].

B. PIV results

The resolution of the PIV diagnostic is approximately four times coarser than the LIF diagnostic. For combined PIV-LIF results, we interpolate the computed PIV vectors onto the LIF grid. However, in this section, we present the PIV results at their original resolution, with no interpolation or filtering.

The rms horizontal and vertical velocity profiles are presented in Fig. 8, together with the uncertainty bands for the statistic (uncertainty here calculated as per [61] with 95% confidence level). u'_{rms} and v'_{rms} profiles differ from a typical Gaussian profile in the fact that they are flat through the core of the mixing region. This implies that the turbulence is of unvarying strength through the majority of the mixing region, except at the edges. In general, the strength of vertical velocity fluctuations is double that of horizontal ones. The exception is for Re = 520, where the horizontal velocity fluctuations are so small as to not be distinguishable from the velocity fluctuations of the free stream.

The vertical rms velocity fluctuation can be used to compute the Reynolds number of the flow. In Eq. (3), the length scale of the flow is chosen to be the total extent of the mixing width, $2h$, and the velocity scale is chosen to be the vertical rms velocity fluctuation v'_{rms}. Together with the mixture viscosity, v, this creates an equation for the Reynolds number, Eq. (7). This is the equation
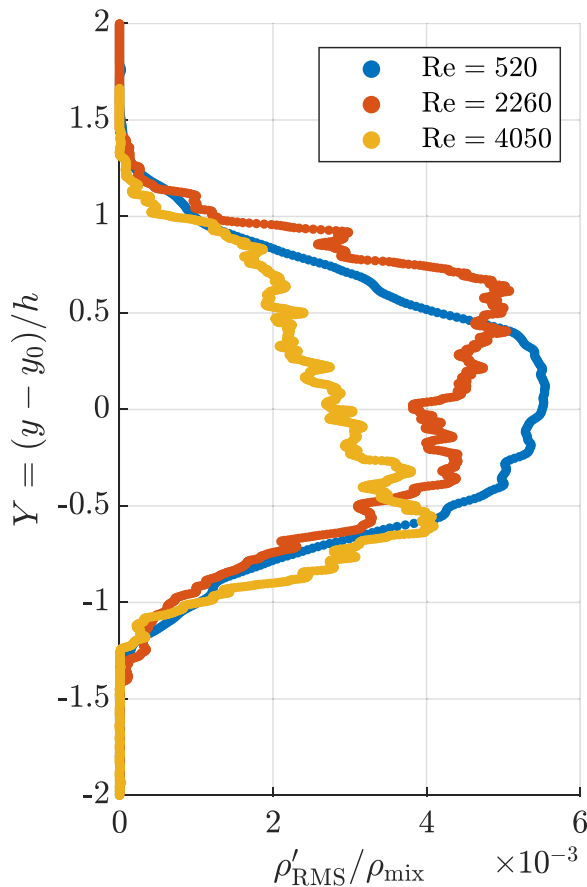
FIG. 7. Normalized profiles of the root-mean-square density fluctuation for the three Reynolds numbers tested.

for Reynolds number that is used to derive the Reynolds numbers presented throughout this paper:

$$\mathrm{Re} = \mathrm{Re}_{v'_\mathrm{rms}} = \frac{2hv'_\mathrm{rms}}{\nu}. \tag{7}$$

One of the primary tests to determine if a flow has entered into a fully turbulent state is to determine if it displays self-similarity in profiles of the velocity and density statistics. In order to verify this, we follow the technique of [34,45] by normalizing the profiles of the rms horizontal and vertical velocity fluctuations with the terminal bubble velocity v_∞ [62]. Figure 9 shows the profiles of the normalized rms horizontal and vertical velocity fluctuations. The figure shows good self-similar collapse for the Re = 2260 and 4050 cases. The Re = 520 case still has not reached the fully turbulent state, and fails to collapse as a result. The plots show that v'_rms/v_∞ has a peak of unity, suggesting that the chosen definition of terminal bubble velocity [62] is an excellent scaling for this velocity. In addition, u'_rms/v_∞ has a peak of around 0.6, illustrating the anisotropic nature of the flow in the core of the mixing region. In order to further validate this scaling, we superimpose the normalized results of [45], which were performed at lower Atwood number and much larger Schmidt number than the current experiment. The good agreement between the two data sets implies that this scaling is insensitive to the strength of molecular diffusion and to Atwood number in the case of Boussinesq flows. To compare to a non-Boussinesq flow, we also superimpose the normalized results of [34]. This experiment shows good collapse for the u'_rms scaling, but not for
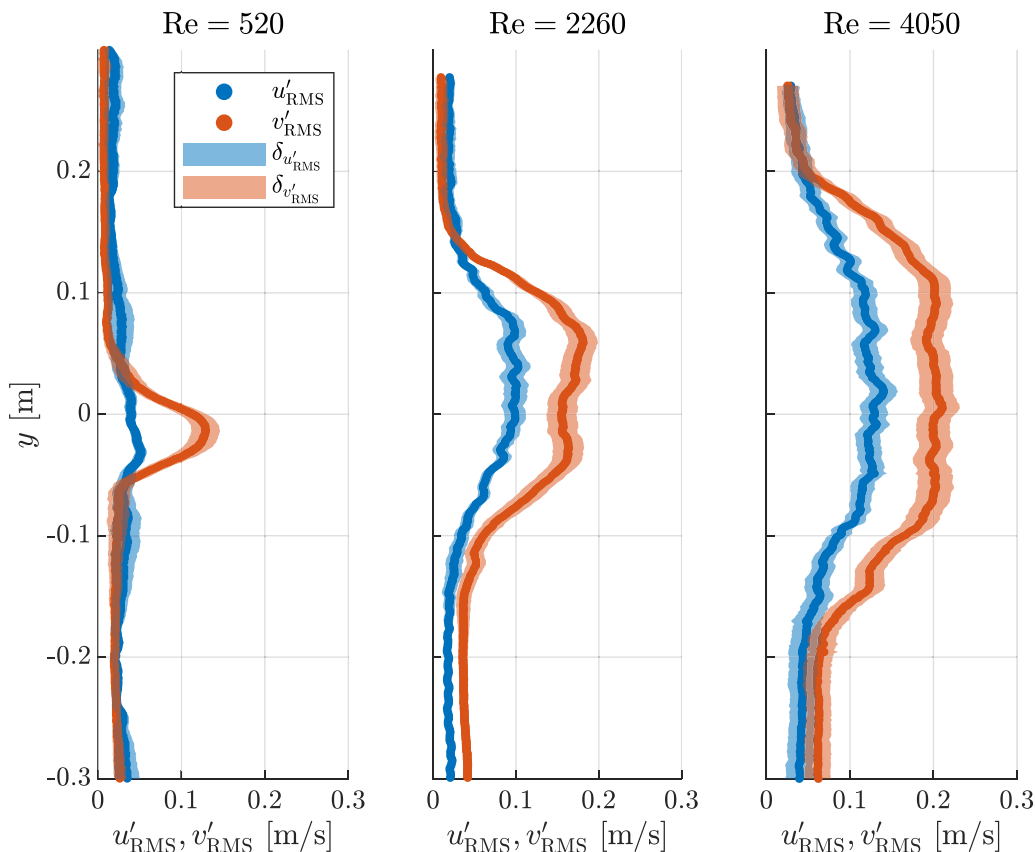
FIG. 8. Profiles of the root mean square of the fluctuation of the horizontal and vertical velocity components, u'_{rms} and v'_{rms}, together with the associated uncertainty in the statistic.

the v'_{rms} scaling. Reference [34] had similarly found that vertical velocity fluctuations were larger than the terminal bubble velocity at large Atwood numbers, potentially resulting from the large velocity of the spike [62], which is asymmetric relative to the bubble at larger Atwood number.

Anisotropy tensor

Some of the most integral theories concerning turbulence, proposed by [63], assume that the turbulence is locally isotropic: in other words, at the smallest scales of the flow, the flow has no recognition of the large-scale boundary conditions and therefore has no preference of direction. Many turbulent flows are anisotropic, with even the smallest scales of the flow showing a directional preference. A measure frequently used to describe the degree of anisotropy is the anisotropy tensor, b_{ij}, which is defined by Eq. (8):

$$b_{ij} = \frac{\overline{u'_i u'_j}}{\overline{u'_k u'_k}} - \frac{\delta_{ij}}{3} \tag{8}$$

where u'_i is the velocity fluctuation vector, δ_{ij} is the Kronecker delta, and repeated subscripts imply Einstein summation convention. b_{ij} may vary from a minimum value of $-1/3$, indicating that none of the energy of the turbulence is contained in that fluctuating component, to a maximum value of $2/3$, indicating that all of the energy of the turbulence is contained in that fluctuating component. In an isotropic flow, all of the components of the anisotropy tensor are zero. For the planar two-
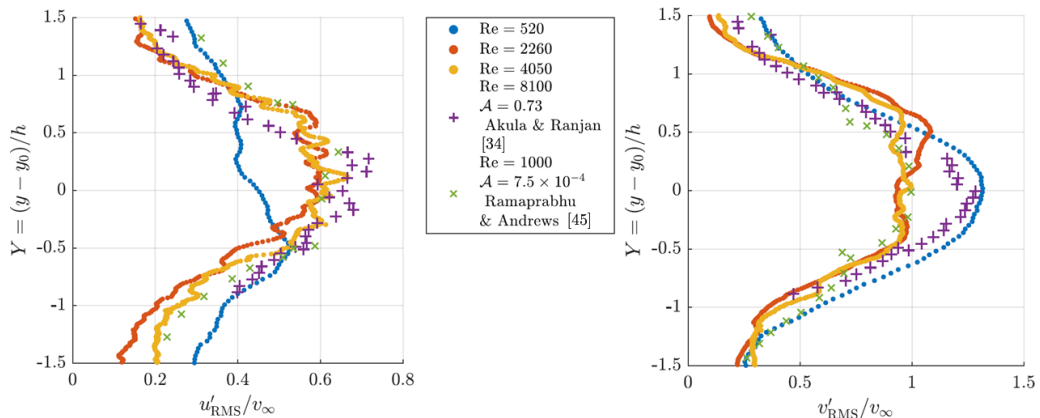
FIG. 9. Profiles of the rms horizontal and vertical velocity fluctuations, normalized by the Goncharov bubble velocity. For comparison, the normalized profiles from [34,45] are also presented.

component PIV measurement recorded here, we do not have the ability to measure velocities in the plane normal direction, w. To replace this term in Eq. (8), we utilize an assumption frequently made in turbulent flows that $w' \approx u'$ [27,45].

Figure 10 shows the profiles of the anisotropy tensor components b_{uu}, b_{vv}, and b_{uv} for the Re = 4050 experiment. The profile shows that there is nearly no energy in the cross-correlation component b_{uv} over the entire mixing width, indicating that the horizontal and vertical velocity fluctuations are mostly uncorrelated. Overall, both b_{uu} and b_{vv} are nearly constant across the entire mixing region, with $b_{uu} \approx -1/6$ and $b_{vv} \approx 1/3$. This indicates that the flow displays a strong but nearly constant anisotropy throughout the entire mixing region.

C. Simultaneous PIV-LIF results

1. Turbulent mass flux

By utilizing the simultaneous results of our PIV-LIF diagnostic, we are able to provide field measurements of cross correlations of the density and velocity. This is necessary for the computation of the turbulent mass flux, a_i. a_i is one of the quantities modeled with a transport equation in the Besnard-Harlow-Rauenzahn (BHR) model [64], as well as a component of the production term in the variable-density turbulent kinetic energy equation. The profiles for $a_y = \overline{\rho' v'}/\overline{\rho}$ for the three Reynolds numbers tested are shown in Fig. 11, along with the associated uncertainty in the statistic (uncertainty here calculated as per [61] with 95% confidence level). The profile of a_y grows in width at a similar rate to the velocity fluctuations. At Re = 4050, a clear asymmetry is seen between the spike side and bubble side, with the spike side having greater turbulent mass flux. Even though the Atwood number of the current experiment is small, and the flow should be relatively Boussinesq, it is possible that there is some asymmetry developing in the shape of the spike, resulting in an increase in turbulent mass flux on the spike side. Through conditional statistics, separating the impact of the bubble and the spike, [34] also found that, at large Atwood numbers, asymmetry led to the increased contribution of the spike to the development of turbulent mass flux. Such an asymmetry and its effects are found to increase with increasing Atwood number [26,34,49].

To further understand the turbulent mass flux, the PDF of the density-velocity correlation $\rho' v'$ is presented in Fig. 12. There is good collapse in the PDF between the two Reynolds numbers shown. Both PDFs show a significant peak at zero, with only a small probability of positive correlation. They exhibit long tails which gradually descend into negative correlation values. When compared to the results of [34] at larger Atwood number, the slope of the negative correlation tail is more gradual
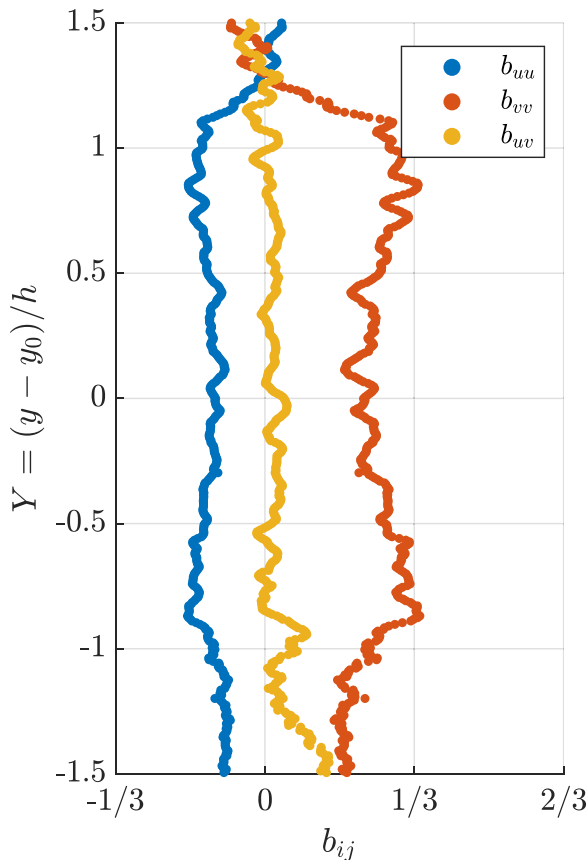
FIG. 10. Profiles of the components of the anisotropy tensor, b_{ij}, for the Re = 4050 experimental case.

and extends to more negative values. The PDF of the density-velocity correlation for smaller than current Atwood number [49] is also shown.

2. Reynolds stress

In addition to the turbulent mass flux, we are able to compute the Reynolds stress components for the compressible RTI flow, $R_{ij} = \overline{\rho u_i'' u_j''}$, where $u_i'' = u_i - \frac{\overline{\rho u_i}}{\overline{\rho}}$ is the Favre-average fluctuating component. From the Reynolds stress tensor components, the turbulent kinetic energy can be computed by dividing half the trace of the tensor by the mean density, so that $k = \frac{1}{2\overline{\rho}}(R_{xx} + R_{yy} + R_{zz})$. We apply the same assumption here as was applied to the anisotropy tensor, that $R_{zz} = R_{xx}$ in the present flow. Figure 13 shows the profiles of the turbulent kinetic energy for the three Reynolds numbers tested, normalized by the square of the self-similar velocity scale, $U_{h_f}^2$, where $U_{h_f} = \sqrt{\mathcal{A}g h_f}$. Reasonable collapse is found, with a peak normalized value of approximately $k/U_{h_f}^2 = 0.1$. More on turbulent kinetic energy is discussed later in the paper.

3. Conditional statistics

The simultaneous measurement of density and velocity allows us to obtain conditional statistics of the data to separate the relative impact of the bubble and spike structures. We follow the work of [34,49] to apply conditional sampling that is focused on the density measurements. Conditional statistics are evaluated for the largest Reynolds number tested, Re = 4050, at the mixing centerline,
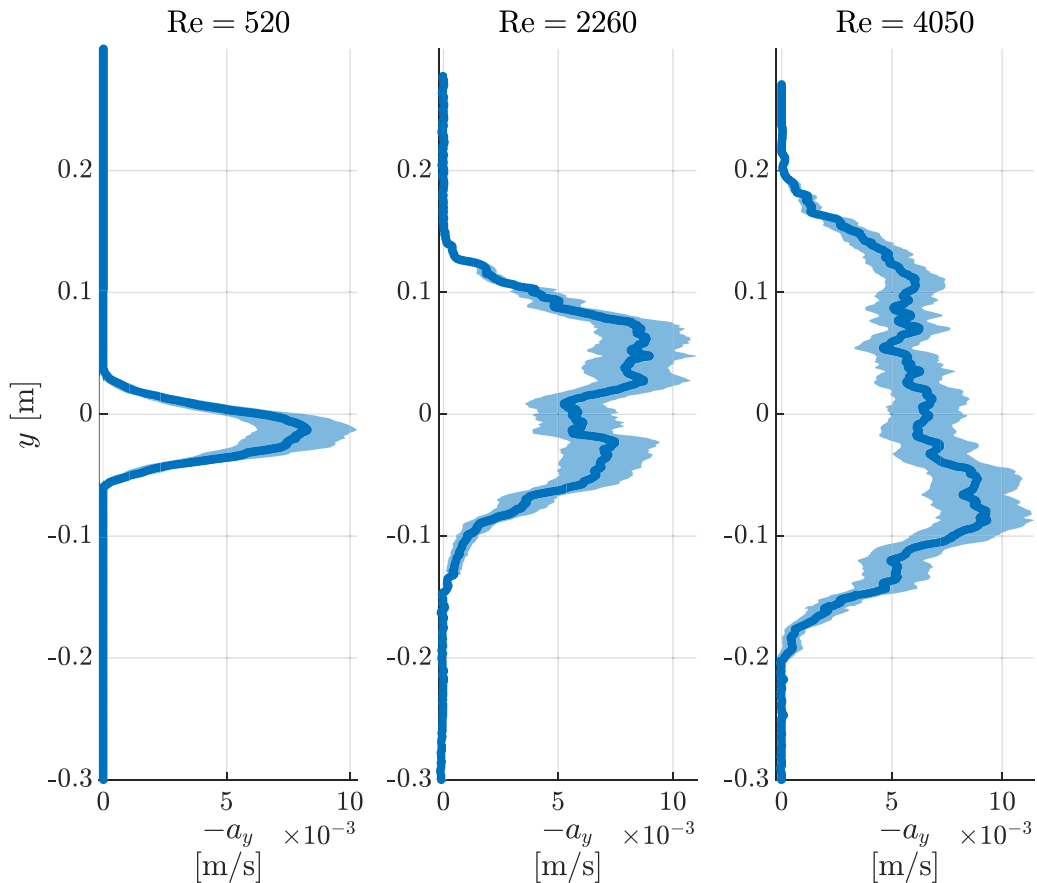
FIG. 11. Profiles of the negative vertical turbulent mass flux, a_y, together with the associated uncertainty in the statistic.

$Y = 0$. At this location, the mean density of the flow, $\overline{\rho}_{\mathrm{mix}}$, is computed and the density fluctuation, ρ', is found by subtracting $\overline{\rho}_{\mathrm{mix}}$ from the instantaneous density measurements. At the mixing centerline, the mean density of the flow is approximately the average of the stream densities so that there are nearly equal components of both stream 1 and stream 2. This being the case, fluid which has a density fluctuation $\rho' > 0$ must have a density greater than $\overline{\rho}_{\mathrm{mix}}$, and is composed primarily of heavy spike fluid. The opposite must be true of fluid with a density fluctuation $\rho' < 0$. This fact allows us to use the sign of ρ' as a condition to separate data associated with the bubble and the spike.

To illustrate the conditional averaging technique, Fig. 14 presents the PDF of ρ' with a dividing line separating $\rho' < 0$ and $\rho' > 0$. These conditions can be used to separate the vertical velocity fluctuations, v', between the bubble and spike contributions. The PDF of v' normalized by the Goncharov bubble velocity is also presented in Fig. 14. It is found that fluid associated with the spike, $\rho' > 0$, primarily has negative velocity fluctuations, with a mean velocity fluctuation being approximately half the bubble velocity. The opposite is true for bubble fluid, $\rho' < 0$. These results agree with the phenomenological view of RTI as the interpenetration of rising and falling fluid, where the direction of the fluid motion is inverse to its relative density. However, it is also clear from these PDFs that there is not one-to-one correspondence between positive density fluctuations and negative velocity fluctuations, nor the opposite for negative density fluctuations. The explanation given by [49] is that this is the result of spike fluid being entrained in vortical rollups by shear
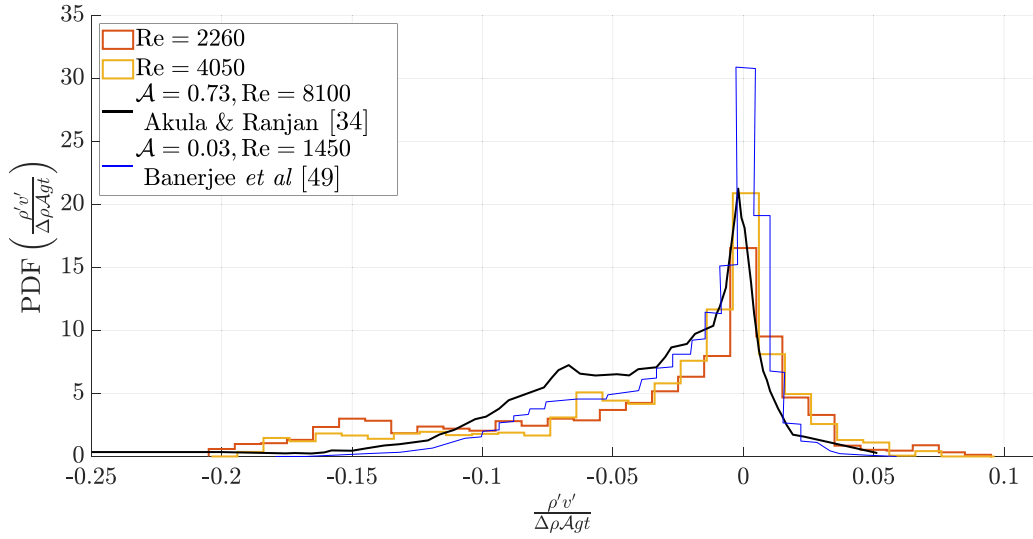
FIG. 12. The probability density function of the density-velocity correlation, $\rho' v'$, after normalization for the Re = 2260 and 4050 cases, evaluated at $Y = 0$. To compare, the density-velocity correlation using the same normalization presented by [34,49] is shown.
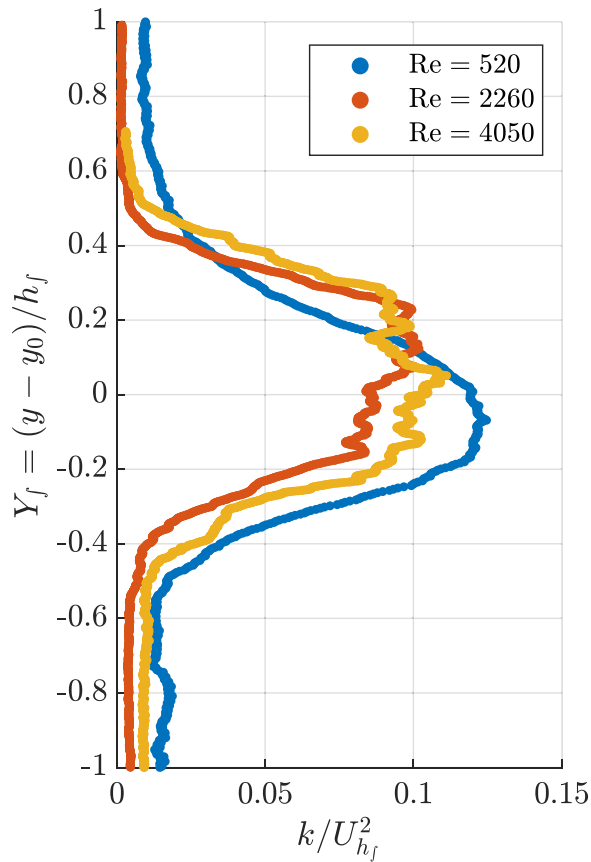

FIG. 13. Profiles of the turbulent kinetic energy, k, normalized by the self-similar velocity scale, U_{h_f}.
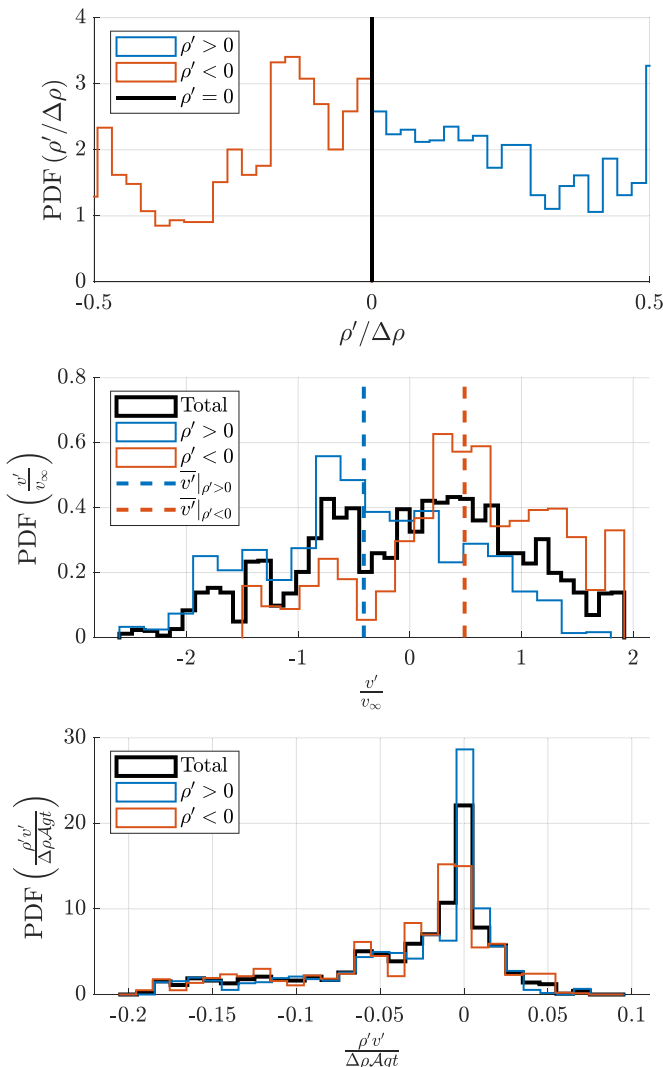
FIG. 14. Probability density functions of the normalized density, velocity, and density-velocity correlation for the sampling conditions $\rho' < 0$ and $\rho' > 0$.

as the bubble and spike move past each other. This entrainment causes the spike fluid to rise with $v' > 0$. The same occurs for the low density bubbles. From observation of the shape of the velocity fluctuation PDF, we also see that the PDF is similar in shape between the two conditions tested. This symmetric nature is expected for this type of low Atwood number flow. To further illustrate the symmetry between the bubble and spike, the PDF of the density-velocity correlation, $\rho'v'$, after conditional separation is also shown in Fig. 14. Again, both PDFs are shown to be nearly identical to each other and similar to the shape of the PDF found using conventional averaging techniques.

While the $\rho' < 0$ and $\rho' > 0$ conditions were useful in separating out the impact of the rising bubbles and falling spikes, it was clear that not all bubble fluid was associated with rising motion, nor spike fluid with falling motion. It may then be useful to condition the flow to separate the impact of rising and falling fluid. This can be accomplished by applying $v' > 0$ and $v' < 0$ as the conditional sampling criteria. Figure 15 shows the PDFs of v', ρ', and $\rho'v'$ when conditioned by the sign of the velocity fluctuation. The PDF of ρ' shown in Fig. 15 explains more clearly the impact of
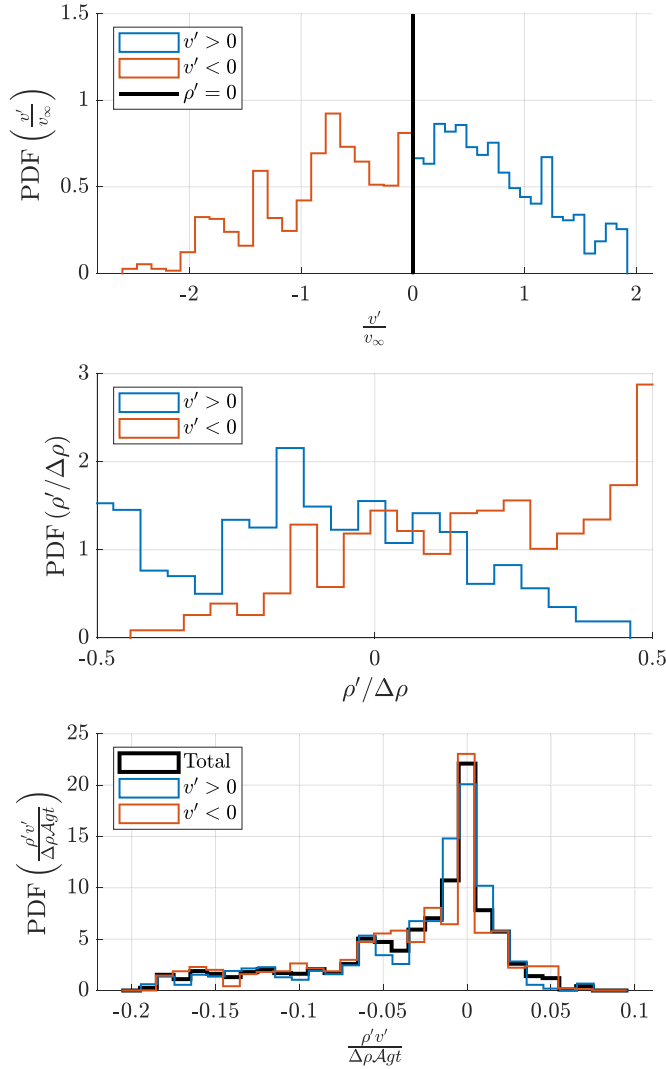
FIG. 15. Probability density functions of the normalized velocity, density, and density-velocity correlation for the sampling conditions $v' < 0$ and $v' > 0$.

entrainment on modulating the velocity fluctuations of fluid of different densities. Both positive and negative velocity fluctuations can carry heavy and light fluid, but the probability of finding heavy fluid moving with positive velocity fluctuation decreases gradually as the density increases. The PDF of $\rho'v'$ in Fig. 15 again shows the symmetric nature of this flow, with the PDFs looking nearly identical to the PDF of the total data set.

Finally, many of the statistics already presented in this paper, such as Reynolds stress, turbulent mass flux, and others, can be recalculated for the conditionally sampled data sets. Table III shows a summary of the measured statistics evaluated using conventional averaging methods, as well as with all four of the conditional sampling techniques that have been described. The general trend of comparison between opposite sampling methods, such as $\rho' > 0$ and $\rho' < 0$, is that the statistics are nearly equal, or else of equal magnitude and opposite sign. This again speaks to the symmetric

TABLE III. Conditional statistics evaluated for the Re = 4050 case at $Y = 0$.

	$\rho' > 0$	$\rho' < 0$	$v' < 0$	$v' > 0$	Conventional
$\overline{f_1}$	0.765	0.306	0.689	0.395	0.533
$\overline{\rho}$ (kgm^{-3})	1.119	1.026	1.104	1.044	1.072
$\overline{u'}$ (ms^{-1})	-0.015	0.015	-0.007	0.006	0.000
$\overline{v'}$ (ms^{-1})	-0.092	0.090	-0.178	0.158	0.000
ρ'_{rms} (kgm^{-3})	0.056	0.057	0.057	0.056	0.056
u'_{rms} (ms^{-1})	0.128	0.116	0.137	0.108	0.122
v'_{rms} (ms^{-1})	0.207	0.197	0.216	0.190	0.202
$\overline{\rho'v'}/\Delta\rho\mathcal{A}gt$	-0.033	-0.032	-0.035	-0.031	-0.033
$a_y = \overline{\rho'v'}/\overline{\rho}$ (ms^{-1})	-0.007	-0.007	-0.007	-0.007	-0.007
$R_{xx} = \overline{\rho u'' u''}$ (kgm^{-1}s^{-2})	0.018	0.014	0.021	0.012	0.016
$R_{yy} = \overline{\rho v'' v''}$ (kgm^{-1}s^{-2})	0.047	0.040	0.050	0.039	0.044
k (m^{2}s^{-2})	0.038	0.033	0.041	0.030	0.036

nature of the bubbles and spikes in this low Atwood number flow. The values in Table III can be compared with the values of conditional statistics in Table 5 of [34] where the pronounced asymmetry due to large Atwood number can be clearly observed. In the present paper, in comparing the conditional sampling techniques between the use of ρ' and v', the values of $\overline{f_1}$ show that the v' sampling method results in fluid that is more homogeneous, with density closer to the mean density of the flow.

D. Measures of molecular mixing

Many RTI phenomena involve miscible fluids which are able to mix at the molecular level at any volume fraction level. In these cases, as the RTI bubble and spike move past one another, unmixed fluid is entrained in the Kelvin-Helmholtz rollups (shear rollups) and other complex features that develop at the interface. The increasing surface area strengthens the impact of diffusion across the interface, eventually leading to molecular mixing. In this section, we provide measures of the molecular mixing in RTI flows. In addition, we quantify the rate of mixing and analyze the processes which lead to the increase of molecular mixing at different locations in the flow.

1. Molecular mixing parameter

Reference [65] quantified molecular mixing as the degree of desegregation of the materials, θ, defined by

$$\theta = 1 - \frac{B_0}{B_2}, \tag{9}$$

$$B_0 = \lim_{T \to \infty} \frac{1}{T} \int_0^T \frac{(\rho - \overline{\rho})^2}{(\Delta\rho)^2} dt, \tag{10}$$

$$B_2 = \overline{f_1}\,\overline{f_2}. \tag{11}$$

θ may take on a value between zero and unity, with zero representing unmixed fluids, and unity representing fluids that are completely molecularly mixed. This technique was first used to study RTI mixing in simulations by [29], and the general trend found in experiments is that $\theta \to 0.75$ in the self-similar regime [25,34,45,49].
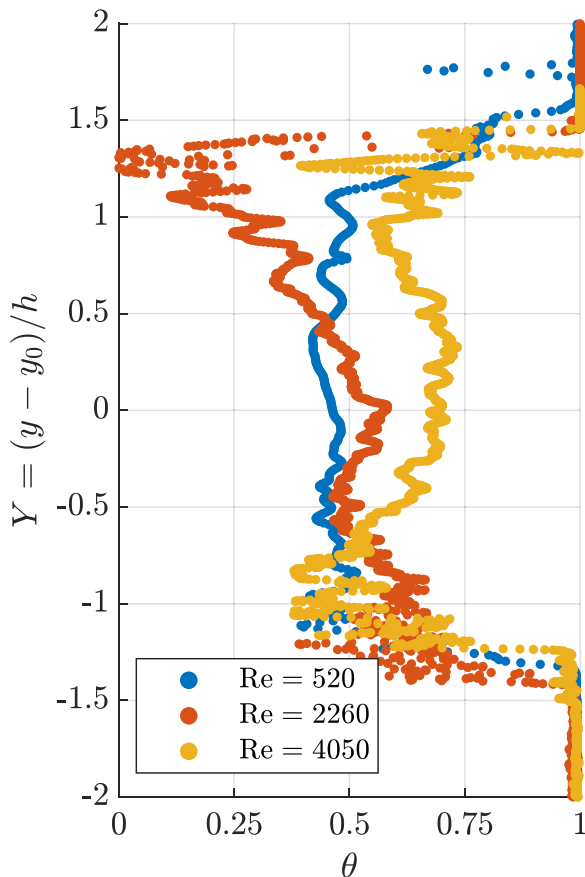
FIG. 16. Profiles of the molecular mixing parameter, θ, for the three Reynolds numbers tested.

The results of our LIF diagnostic equip us with measurements of the volume fraction and density across the mixing region, allowing us to compute B_0, B_2, and θ. Figure 16 shows the profiles of mixing parameter, θ, across the normalized y coordinate for the three Reynolds numbers tested. In the core of the mixing region, θ proceeds from a value of around 0.45 at the lowest Reynolds number to around 0.7 at the largest Reynolds number. This shows that the degree of desegregation in the core of the flow is approaching the expected asymptote of 0.75.

2. Density-specific-volume correlation

An important mixing measurement that is used frequently in turbulence modeling is the density-specific-volume correlation, $b = -\overline{\rho'(\frac{1}{\rho})'}$. b can be thought of as a measure of potential for future mixing and varies from a value of zero, representing a perfect mixture, to $b_{\max} = \overline{f_1}\,\overline{f_2}\frac{(\rho_1-\rho_2)^2}{\rho_1\rho_2}$, representing completely unmixed fluids. The dependence of $b_{\max}$ on $\overline{f_1}$ and $\overline{f_2}$ suggests that it is not a constant over the width of the mixing region. Also notice that b is inherently dimensionless. The definition of b shown is the simplest to describe, but it can be algebraically manipulated to be described in alternative ways. One of these most useful alternatives is the recognition that $b = \overline{(\rho'\rho')/\rho\overline{\rho}}$, showing that b is closely related to the mean square of the density fluctuation.
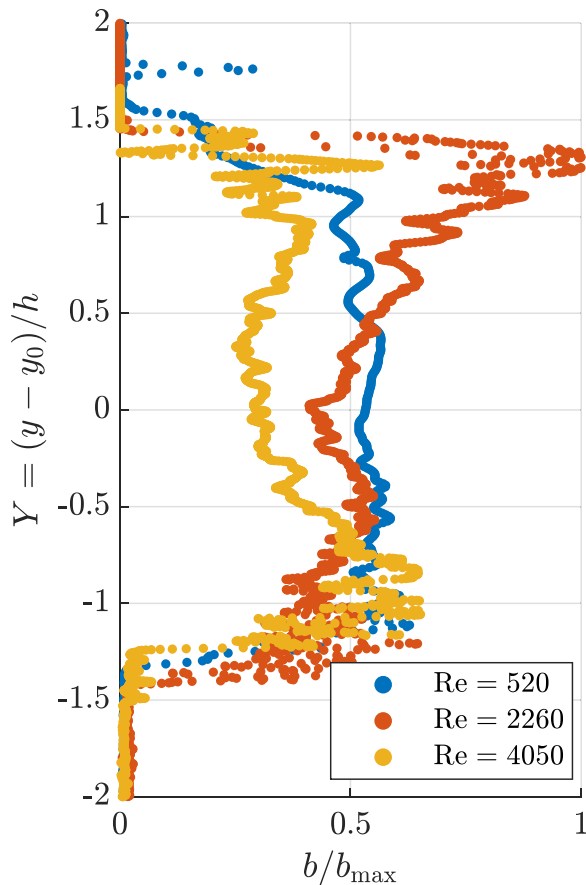
FIG. 17. Profiles of the density-specific-volume correlation, b, normalized against the maximum possible value of b given the volume fractions present at the spatial location, $b_{\max}$.

Figure 17 shows the normalized profiles of b based on normalization by $b_{\max}$. The normalization results in a b profile that is nearly constant through the entire mixing region, with only moderate peaks near the edges of the mixing region. It also shows that $b/b_{\max}$ approaches a value of 0.3 at the center of the mixing region. This normalized b profile changes the perspective of how the potential for mixing varies across the mixing region. Rather than viewing the potential for mixing as being maximized at the mixing centerline, it is more consistent with the results to view it as being nearly constant throughout the entire mixing region, and being mostly limited by the relative concentrations of the fluids being mixed.

3. Density-specific-volume correlation evolution equation budget

By manipulating the Reynolds-averaged continuity equation, it is possible to arrive at the transport equation for b, such as in the analysis technique of [64]. One form of this transport equation is Eq. (12):

$$\underbrace{\frac{\partial b}{\partial t} + \tilde{u}_j \frac{\partial b}{\partial x_j}}_{\text{T1. Advection}} = \underbrace{2a_j \frac{\partial b}{\partial x_j}}_{\text{T2. Convection}} - \underbrace{2a_j \frac{1+b}{\overline{\rho}} \frac{\partial \overline{\rho}}{\partial x_j}}_{\text{T3. Production}} + \underbrace{\overline{\rho} \frac{\partial}{\partial x_j} \left[\frac{\overline{u_j' \rho'(1/\rho)'}}{\overline{\rho}} \right]}_{\text{T4. Transport}} + \underbrace{2\overline{\rho} \, \overline{\left(\frac{1}{\rho}\right)' \frac{\partial u_j'}{\partial x_j}}}_{\text{T5. Decay}} \quad (12)$$
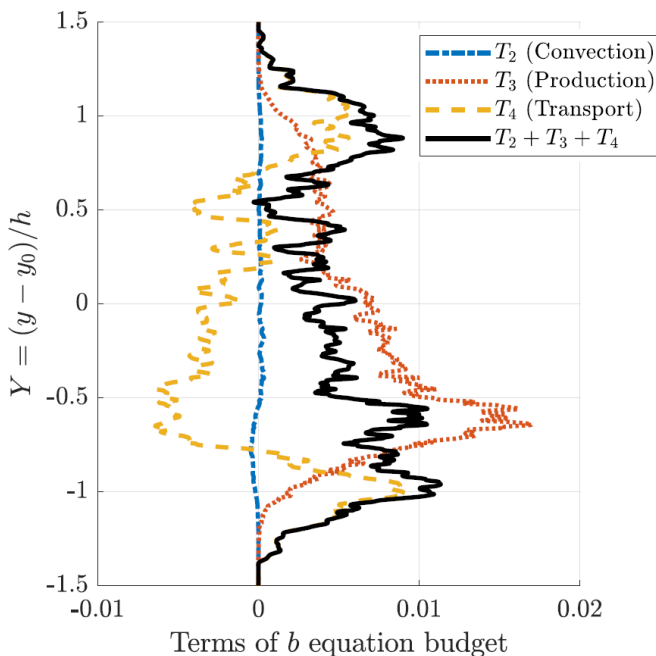
FIG. 18. Profiles of the terms of the density-specific-volume correlation evolution equation budget, T2, T3, T4, and their sum for the Re = 4050 case.

where repeated subscripts indicated Einstein summation notation. In the current statistically stationary flow, the unsteady term $\frac{\partial b}{\partial t}$ is zero. This leaves term T1, the advection of b, as the only term on the left hand side. For this "convective-type" facility, it can be shown that the x gradient of the advection term is exactly equal to the unsteady term in an equivalent "box-type" facility with homogeneous initial condition through the application of Taylor's hypothesis.

On the right hand side of Eq. (12), term T5 is related to the decay of b due to diffusion and is generally small for subsonic flows [64]. This leaves the important terms describing the convection, production, and transport of b, terms T2, T3, and T4, as being the primary terms determining the budget of b. For the conditions of the current flow, $a_x \approx a_z \approx 0$, leading to a significant simplification for terms T2 and T3. The evaluation of term T4 unfortunately requires us to compute the x-direction gradient, which is unavailable with the current LIF diagnostic limitations, but it is reasonable to assume that gradients in the x direction will be small relative to the gradients across the mixing region. These assumptions allow us to measure the budget of b across the mixing region, a measurement first performed by [66].

Figure 18 shows the profiles of the terms in the b evolution equation budget for the Re = 4050 case. The budget shows a relatively small contribution from convection over the entire mixing width. Production is found to be asymmetric, being primarily centered in the spike. This helps to answer the question of why the b profile seems to be asymmetric across the mixing region, with increased values of b in the spike region. It is clear that b is being produced at a greater rate in this region of the flow. Generally, production of b is found to be the primary contributor to the b budget, being nearly equal to the advected b everywhere except at the edges of the mixing region.

The transport term changes sign as it varies from the edges of the mixing region, where it is positive, to the core of the mixing region, where it is negative. It is also interesting to note that, while production rapidly vanishes to zero at the edges of the mixing region, $Y = \pm 1$, transport reaches a peak at these locations. This implies that the spatial growth of the b profile is solely due to the transport of b away from the core of the mixing region by the large-scale motion of the

TABLE IV. Details on the measured changes in potential energy, turbulent kinetic energy, and dissipated energy for the three Reynolds numbers studied.

Re	ΔPE mJm^{-2}	ΔKE mJm^{-2}	D mJm^{-2}	$\frac{\Delta\text{KE}}{\Delta\text{PE}}$	$\frac{D}{\Delta\text{PE}}$
520	0.49	0.47	0.02	0.96	0.04
2260	5.25	3.72	1.53	0.71	0.29
4050	11.57	7.10	4.47	0.61	0.39

bubble and spike, and not by the production of b at these locations. Together, the behaviors of the production and transport profiles show the balance taking place between production of b at the core of the mixing region and the transport of b to the outer edges of the flow.

E. Energy transfer in the Rayleigh-Taylor instability

1. Potential energy release

RTI leads to the release of gravitational potential energy stored in the density stratification as the heavy and light fluids displace each other. This released energy is converted into kinetic energy which, for a turbulent flow, is decomposed into the turbulent kinetic energy, k, and the kinetic energy of the mean flow. This conversion is not perfect, and some energy is lost as heat through viscous dissipation. Following the methodology of [67], we desire to know what fraction of the released potential energy is converted into turbulent kinetic energy based on the simultaneous measurements of the density and velocity fields.

At any downstream location, x, the gravitational potential energy per unit width, PE(x), can be measured by integrating the density profile at that x location across the entire y domain of the gas tunnel, which spans from $-H/2$ to $H/2$, where H is the height of the gas tunnel facility test section. This results in $\text{PE}(x) = \int_{-H/2}^{H/2} \rho g y \, dy$. Meanwhile, the kinetic energy per unit width, KE(x), can be found by integrating the turbulent kinetic energy profile multiplied by the density profile across the y domain, as $\text{KE}(x) = \int_{-H/2}^{H/2} \rho k \, dy$ where $k = \frac{1}{2\rho}(R_{xx} + R_{yy} + R_{zz})$, and $R_{ij} = \overline{\rho u_i'' u_j''}$. We again make the assumption that $R_{zz} = R_{xx}$ in this flow. Because the mean flow of the gas tunnel is assumed to be fully developed and invariant with streamwise distance, x, we consider the change in the kinetic energy of the mean flow to be negligible.

The density profile and kinetic energy profile at the initial condition, $x = 0$, are based on a step change in density and free-stream kinetic energy values, respectively [54]. These profiles can then be integrated to obtain the initial gravitational potential energy and turbulent kinetic energy, PE_0 and KE_0, respectively. At each measured downstream location x and associated Reynolds number, the potential energy released can then be calculated as $\Delta\text{PE}(x) = \text{PE}_0 - \text{PE}(x)$, whereas the increase in turbulent kinetic energy can be calculated as $\Delta\text{KE}(x) = \text{KE}(x) - \text{KE}_0$. The dissipated energy D is calculated as the remainder of the potential energy release which is not converted into turbulent kinetic energy $D(x) = \Delta\text{PE}(x) - \Delta\text{KE}(x)$.

The $\Delta\text{KE}/\Delta\text{PE}$ and $D/\Delta\text{PE}$ ratios for the three Reynolds numbers are reported in Table IV. At early instability mixing times, nearly all of the potential energy released is converted into kinetic energy in the flow. At this early instability time there is little shear present at the interface, preventing viscosity from being able to effectively dissipate the velocity variations. However, as the Reynolds number increases and shear between the bubble and spike structures begins to grow, the strength of dissipation also increases until the dissipation accounts for nearly 38% of the total released potential energy. This value is low compared to the simulation results of [67], which found $D/\Delta\text{PE} \approx 0.52$, and is also low compared to the simultaneous density-velocity point measurements captured by [45], which found $D/\Delta\text{PE} \approx 0.49$. Together with the normalized kinetic energy profile shown in Fig. 13, these results imply that the turbulent kinetic energy in our flow is greater than previous RTI mixing

experiments. Potential reasons for this could be underestimating initial kinetic energy and presence of mean shear as part of our experimental setup.

2. Turbulent kinetic energy evolution equation budget

Most RANS-type turbulence models, such as the $k - \epsilon$ model and the BHR model [64], rely on the accurate modeling of the transport of turbulent kinetic energy, k. The compressible transport equation for k can be presented as Eq. (13) [64,68,69]:

$$\frac{\partial}{\partial t}(\overline{\rho} k) + \underbrace{\frac{\partial}{\partial x_i}(\tilde{u}_i \overline{\rho} k)}_{C^k} = \underbrace{-R_{ij}\frac{\partial \tilde{u}_i}{\partial x_j} + a_i \frac{\partial \overline{p}}{\partial x_i}}_{P^k} \underbrace{- a_i \frac{\partial \overline{\tau}_{ij}}{\partial x_j}}_{M^k} + \underbrace{\overline{p'\frac{\partial u_i''}{\partial x_i}}}_{\Phi^k} + \underbrace{\frac{\partial}{\partial x_j}\overline{u_i''\tau_{ji}'}}_{\tau^k} - \underbrace{\frac{1}{2}\frac{\partial}{\partial x_j}R_{jii}}_{D^k} - \underbrace{\frac{\partial}{\partial x_i}\overline{u_i''p'}}_{\Pi^k}$$
$$\underbrace{- \overline{\tau_{ji}'\frac{\partial u_i''}{\partial x_j}}}_{\epsilon^k} \tag{13}$$

where $k = \frac{1}{2\overline{\rho}}R_{ii}$ and $R_{ij} = \overline{\rho u_i'' u_j''}$ are the turbulent kinetic energy and Reynolds stress, respectively, both defined as they are elsewhere in this paper, $R_{ijk} = \overline{\rho u_i'' u_j'' u_k''}$ is the velocity-triple-correlation term, $a_i = \overline{\rho' u_i'}/\overline{\rho}$ is the turbulent mass flux, and τ_{ij} is the viscous stress tensor for a Newtonian fluid. The notation used for Reynolds and Favre averaging elsewhere in this paper is also applied to this equation. Here, we quantify these terms using the collected PIV-LIF data at Re = 4050.

In order to compute the k budget from the current experiment, several assumptions about our underlying flow must be made, like time derivatives of mean quantities being zero, derivatives of mean quantities in the z direction being zero, etc. [54]. Certain terms of the k budget require the computation of gradients in the x and y directions. To estimate these x gradients, we assume that the flow has reached a self-similar state by the Re = 4050 location. For a temporally evolving RTI flow, the similarity variable, η can be found in terms of the location across the mixing region, y, and the mixing width, $h(t^2)$, as $\eta = y/h$. By substituting the temporal evolution of h, and recognizing the application of Taylor's hypothesis in the current flow, this allows us to find a similarity variable to describe the gas tunnel facility flow, $\eta = y/x^2$. Using this similarity variable, various profiles computed for the flow at location x can be recast in terms of their evolution with time ($t = x/U$ in the current convective flow), and a self-similar equation only dependent on η. In other words, for every measured quantity $\phi(x, y)$, we apply a self-similar transformation to recast $\phi(x, y) = x^n\hat{\phi}(\eta)$, where the exponent n depends on the growth rate of the quantity ϕ in space. Based on the determined PIV results, and the self-similarity scalings applied by other authors [55], we can assume that Reynolds stresses and the turbulent kinetic energy follow a quadratic scaling, $n = 2$, velocity-triple-correlation terms follow a cubic scaling, $n = 3$, and turbulent mass flux follows a linear scaling. The density profile is already assumed to be self-similar, so that $n = 0$. The result of this analysis is the formation of a group of self-similar profiles, $\hat{R}_{ij}$, $\hat{k}$, $\hat{R}_{ijk}$, $\hat{a}_i$, and $\hat{\rho}$ such that

$$R_{ij}(x, y) = x^2\hat{R}_{ij}(\eta),$$
$$k(x, y) = x^2\hat{k}(\eta),$$
$$R_{ijk}(x, y) = x^3\hat{R}_{ijk}(\eta),$$
$$a_i(x, y) = x\hat{a}_i(\eta),$$
$$\overline{\rho}(x, y) = \hat{\rho}(\eta).$$

The self-similar profiles are found from the measurements of the profiles at the $x = 1.75$ m, Re = 4050 location and can be linearly interpolated to find their value at any value of η.

With the self-similar profiles in hand, gradients of a quantity ϕ in the x direction can be found by applying a first-order central-difference scheme. To increase the accuracy of the gradient, small
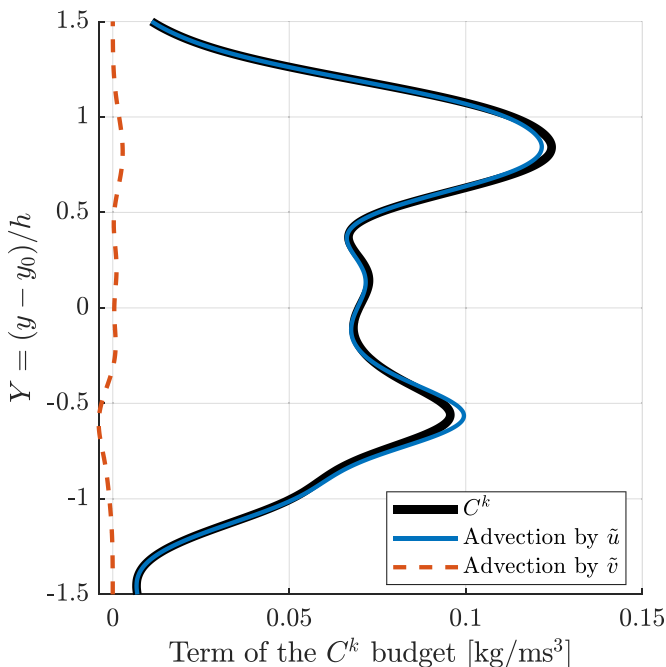
FIG. 19. Profile of the advection term, C^k, and the relative contributions of the horizontal and vertical gradient terms.

values of Δx should be used. Specifically, we choose for Δx to equal the y resolution of the LIF measurement so that $\Delta x = \Delta y$. Gradients in the y direction are also found using a central-difference scheme. Finally, in order to reduce the noise in the gradients, a Gaussian filter of 5-cm window size is used to reduce the strength of high-frequency fluctuations in the profiles of the measured quantities before the central-difference derivatives are computed. The measurements of the grouped terms in Eq. (13) are iterated below.

The first term on the left hand side is the unsteady term, which is zero for the statistically stationary flow of the gas tunnel facility. The second term on the left hand side, C^k, represents the advection of turbulent kinetic energy, and for the current flow it simplifies to

$$C^k = \frac{\partial}{\partial x}(\tilde{u}\overline{\rho}k) + \frac{\partial}{\partial y}(\tilde{v}\overline{\rho}k). \tag{14}$$

It can be shown that the first term of $C^k = \frac{\partial}{\partial x}(\tilde{u}\overline{\rho}k) = \frac{\partial t}{\partial x}\frac{\partial}{\partial t}(\tilde{u}\overline{\rho}k) = \frac{1}{U_c}\frac{\partial}{\partial t}(U_c\overline{\rho}k) = \frac{\partial}{\partial t}(\overline{\rho}k)$ is identically equal to the unsteady term for the typical "box-type" RTI experiment when Taylor's hypothesis is applied. Figure 19 shows the profile for C^k, as well as the contributions of the horizontal and vertical gradient. As expected, the horizontal gradient, which represents the total growth rate of k, is dominant with the vertical gradient only providing a small effect. The advection peaks at the inner edge of the mixing width, around $Y \approx \pm 0.7$, indicating that the major growth in turbulent kinetic energy in the flow occurs at the edges of the mixing region, and not in the center. The advection also extends far beyond the mixing width, indicating that the RTI serves to increase the turbulent kinetic energy of the flow even in the free stream through large-scale motions of the bubbles and spikes.
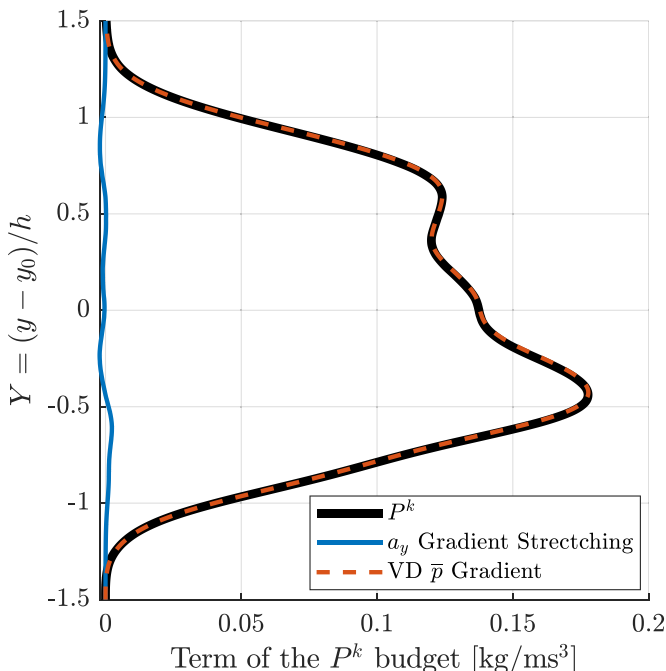
FIG. 20. Profile of the production term, P^k, and the relative contributions of the velocity gradient stretching term and the variable-density pressure gradient term.

The first group of terms on the right hand side of Eq. (13) is P^k, which represents the production of turbulent kinetic energy. With the assumptions made, the production term simplifies to

$$P^k = -R_{yy}\frac{\partial a_y}{\partial y} + a_y\frac{\partial \overline{p}}{\partial y}. \tag{15}$$

The first term on the right hand side represents the production of turbulence due to the stretching of velocity gradients by the velocity fluctuations. The second term represents the production of turbulence due to the interaction between the pressure gradient and the turbulent mass flux fluctuations. To estimate pressure gradient, we note that the major contribution to variation of pressure in the RTI framework is the hydrostatic pressure increase due to gravitational acceleration. This provides a measure for $\frac{\partial \overline{p}}{\partial y} = -\overline{\rho}g$. Figure 20 shows the profile of the production term, as well as the relative contribution of the velocity gradient and variable-density pressure gradient terms. Because velocity gradients are relatively weak, we find that the production due to velocity gradients is small in this flow. This is one way in which RTI contrasts with a shear-driven instability flow, in which this term is the dominant production term. Meanwhile, due to the large values of a_y and the strong hydrostatic pressure gradient, the variable-density pressure gradient term is the dominant production term. While there is a peak in the production at $Y \approx -0.5$, the production is relatively uniform across the entirety of the mixing core, and proceeds past the mixing width, h.

The second group of terms on the right hand side of Eq. (13) is M^k, which represents the molecular shearing effect. For the current flow with no mean shear, M^k is identically zero. The third group of terms, Φ^k, which represents the pressure strain effect, can be thought of as the flow work applied by the turbulent fluctuations. In subsonic flows like ours, the divergence of the Favre averaged velocity fluctuations is nearly zero and Φ^k is negligible.

The next three terms in Eq. (13) which are all represented as a gradient of a mean quantity are the transport terms. Because the integral of these terms across the flow volume is identically zero, these
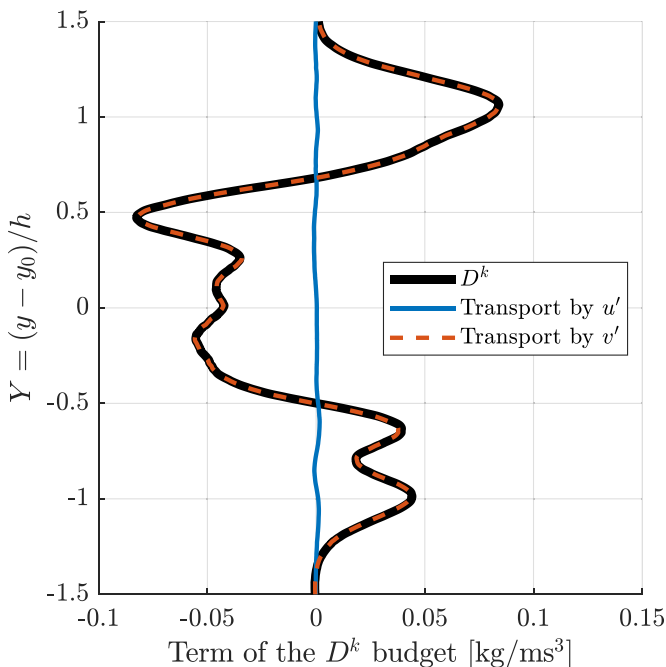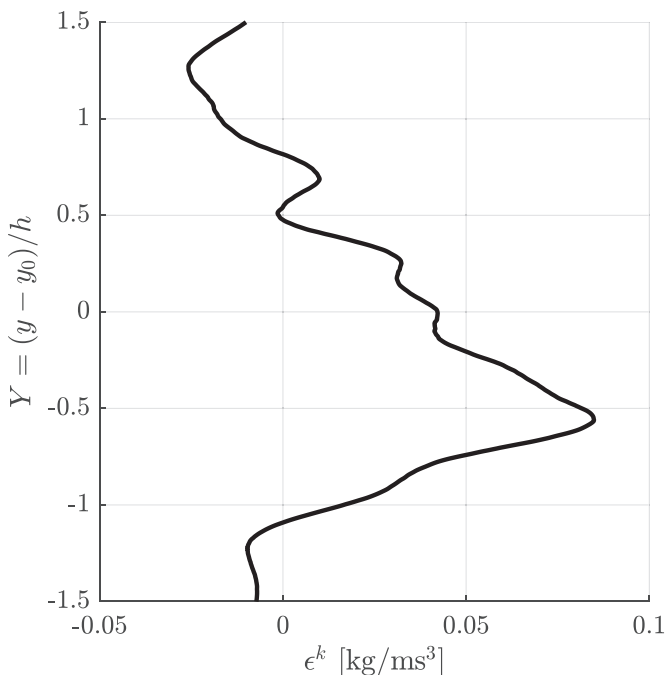
FIG. 21. Profile of the turbulent transport term, D^k, and the relative contributions of the horizontal and vertical velocity fluctuations.

terms represent the movement and redistribution of turbulent kinetic energy around the flow domain, rather than its production or destruction. The first of these terms, τ^k, represents the transport of k by viscous forces, and is generally considered to be small in large Reynolds number flows [69–71]. The major contributor towards transport of k is the term D^k, which represents the transport of turbulent kinetic energy by velocity fluctuations. It is this term which involves the velocity-triple-correlation term, and for the current flow it can be simplified to

$$D^k = -\frac{1}{2}\left[\frac{\partial}{\partial x}(R_{xxx} + R_{xyy} + R_{xzz}) + \frac{\partial}{\partial y}(R_{yxx} + R_{yyy} + R_{yzz})\right]. \tag{16}$$

The equation for D^k shows that it can be decomposed into the contribution of the horizontal and vertical velocity fluctuations towards the transport of k. For an RTI flow which is dominated by vertical velocity fluctuations, we suspect that the vertical velocity fluctuations will be most responsible for turbulent transport. This is confirmed when inspecting Fig. 21, which shows the profile of the turbulent transport term, as well as the relative contributions of the horizontal and vertical velocity fluctuations. Overall, horizontal velocity fluctuations have nearly no effect on the transport of turbulent kinetic energy. When considering the total transport, we find a structure similar to the transport term for b, in which k is moved away from the core of the mixing region and deposited at the edges, near $Y = \pm 1$. The result is that, even though the production of turbulent kinetic energy is dominated at the core of the mixing region, k in this region is quickly transported in a way that leads to dominant advection at the edges of the mixing region, not at the center. It is this transfer process that results in the growth of the RTI mixing width and the transfer of turbulence into the free stream.

The final transport term, Π^k, represents the transport of k due to pressure fluctuations and requires the measurement of pressure fluctuations throughout the flow. In general, most experiments are not able to solve for this term. Reference [72] proposes a model for the pressure transport in terms of the

FIG. 22. Profile of the dissipation, ϵ^k.

turbulent transport, $\Pi^k = -2/5D^k$, which is the model used for this analysis and by [69]. This model is qualitatively accurate except at near-wall conditions where the presence of the wall suppresses pressure fluctuations dramatically faster than velocity fluctuations, leading to an imbalance between the two.

The final term in Eq. (13) is ϵ^k, the dissipation of turbulent kinetic energy. In general, the computation of this term requires the measurement of velocity gradients down to the smallest dissipative scales in the flow, the Kolmogorov microscale, η. This would not be possible considering the diagnostic limitations of our PIV setup. However, we are able to provide an estimate for the dissipation by filling in the remaining terms in the k evolution equation and solving for dissipation, leading to the equation

$$-\epsilon^k \approx C^k - P^k - D^k - \Pi^k. \tag{17}$$

Figure 22 shows the profile for the dissipation across the mixing region. Most importantly, we find that there are places in the flow where the dissipation is not positive, implying that viscous action is leading to an increase in kinetic energy. This is unphysical, and simply related to the limitations in the current technique for measuring x derivatives. Because the advection term is found using a self-similarity argument, which is invalid at the far edges of the flow, it does not take on the negative value it should take in these regions where only dissipation is present. The result is that the dissipation does not take on a positive value, indicating the loss of advected k, and instead has negative value acting as the mechanism that keeps the advected k positive. Despite this limitation, the profile for ϵ^k still provides insights into the mechanism of viscous action in the flow. The dissipation is greater at the core of the mixing region when compared to the edges, suggesting that it is dominant in the regions where shear between the bubble and spike structures is occurring.

Finally, Fig. 23 shows the overlayed profiles of the terms for the turbulent kinetic energy evolution equation. The first trend to observe is that the advection of the flow, C^k, is primarily maintained by the production of turbulent kinetic energy, P^k, nearly everywhere in the flow. This indicates
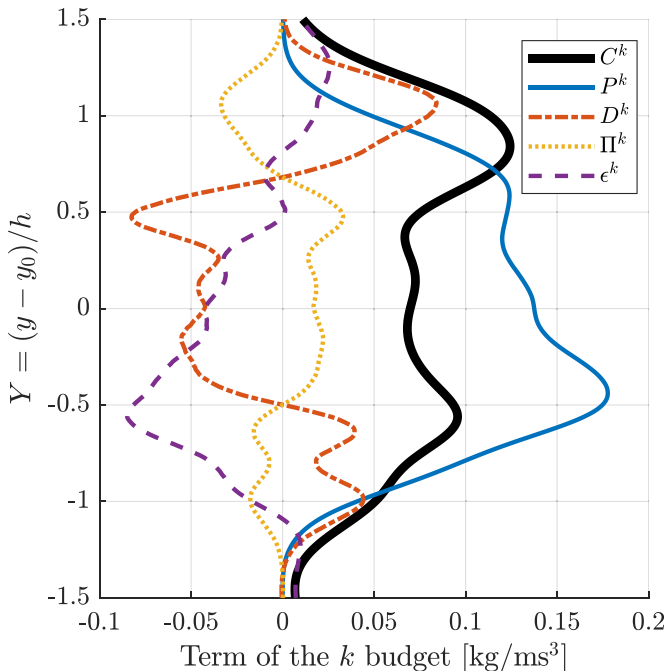
FIG. 23. Profiles of the terms of the k budget, evaluated for the Re = 4050 case.

that although there are many mechanisms which affect k, the primary driver is the production of k, specifically through the release of potential energy. The interaction between the production and the transport of turbulent kinetic energy, D^k, is also important to note here. In general, transport serves to move k away from the core of the mixing region, where the production is dominant, to the edges where it is weaker. As seen when analyzing the budget of D^k, the primary mechanism for this transport is vertical velocity fluctuations associated with the large-scale motion of the bubble and spike. This is the dominant process at the edges of the mixing region. This implies that the growth of the turbulent mixing region in RTI flows is primarily the result of the transport of k.

As shown in Fig. 23, the production and dissipation of turbulent kinetic energy are not balanced in RTI flows. It is this imbalance, with production exceeding dissipation, that leads to the overall growth of the instability, resulting in a positive advection term. Despite this imbalance, the shapes of the dissipation and production profiles have similarities, with both peaking around $Y = -0.5$. The implication is that, in regions of the flow where the production is greater than can be transported away, a stronger dissipation process serves to normalize the level of k growth.

IV. CONCLUSIONS

Simultaneous density-velocity field measurements are captured for the Rayleigh-Taylor instability using a combined PIV-LIF diagnostic. Measurements are captured at Atwood number $\mathcal{A} \approx 0.1$ at three Reynolds numbers, Re = 520, 2260, and 4050.

The statistically stationary nature of the gas tunnel facility allows for the computation of statistical quantities with small experimental uncertainty. From the LIF data, the growth rate parameter is found to be $\alpha = 0.049$. When normalized by the integral mixing width, the volume fraction profile shows good collapse across all Reynolds numbers, with the shape being similar to a linear variation in the mixing region.

Velocity measurements are captured using the PIV diagnostic. The root-mean-square velocity fluctuation profiles show flat peaks through the core of the mixing region, indicating the

homogeneous nature of the turbulence in the core. When normalized by the Goncharov bubble velocity, the velocity profiles show good self-similar collapse and agreement with the low Atwood number data in the literature. There is significant anisotropy in the flow, with horizontal velocity fluctuations being only 60% of the vertical velocity fluctuations. This degree of anisotropy is uniform across the mixing region.

The simultaneous PIV-LIF diagnostic allows the computation of correlated quantities of density and velocity. The profile of the turbulent mass flux shows asymmetry in the development of the instability, with increased turbulent mass flux in the spike. The result is a larger production of turbulence in the spike region. However, such an asymmetry and its effects are more pronounced at higher Atwood numbers. The simultaneous density-velocity measurements allow us to apply conditional sampling techniques to isolate the relative impact of the bubble and the spike on the statistics.

Molecular mixing in the RTI flow is studied by calculating the molecular mixing parameter and the density-specific-volume correlation term b. The molecular mixing parameter at the core of the flow increases with Reynolds number towards an asymptotic value of 0.75. The profiles of the density-specific-volume correlation show that it takes on a nearly constant peak value regardless of Reynolds number. An analysis of the transport equation of the density-specific-volume correlation shows that production is the dominant mechanism in the core of the mixing region, while transport is primarily responsible for the movement of b to the edges of the flow.

An analysis of the turbulent kinetic energy produced and gravitational potential energy released shows that the ratio of dissipated energy to potential energy released is 38% at the largest Reynolds number. The budget of the turbulent kinetic energy, k, is studied term by term. Advection is found to be maximum at the edges of the mixing region, and not at the core, suggesting that the outward growth of the instability is stronger than the maintenance of turbulence in the core. Production is found to be dominated by the variable-density pressure gradient term and not by velocity gradient stretching. Transport is found to be dominated by the movement of k through large-scale vertical motions of the bubble and spike. It is through the transport that the strong advection at the edges of the mixing region is maintained. Dissipation is found to increase proportionally to the rate of production, serving as a balancing mechanism.

ACKNOWLEDGMENT

[1] S. Woosley and T. Weaver, The physics of supernova explosions, Annu. Rev. Astron. Astrophys. **24**, 205 (2002).

[2] E. Mueller and W. D. Arnett, Carbon combustion supernovae: Numerical studies of the final evolution of degenerate carbon-oxygen cores, Astrophys. J. **307**, 619 (1986).

[3] E. Livne and D. Arnett, On the instability of deflagration fronts in white dwarfs, Astrophys. J. **415**, L107 (1993).

[4] M. Zingale, S. E. Woosley, C. A. Rendleman, M. S. Day, and J. B. Bell, Three-dimensional numerical simulations of Rayleigh-Taylor unstable flames in type Ia supernovae, Astrophys. J. **632**, 1021 (2005).

[5] B. Musci, S. Petter, G. Pathikonda, B. Ochs, and D. Ranjan, Supernova Hydrodynamics: A Lab-scale Study of the Blast-driven Instability Using High-speed Diagnostics, Astrophys. J. **896**, 92 (2020).

[6] J. R. Freeman, M. J. Clauser, and S. L. Thompson, Rayleigh-Taylor instabilities in inertial-confinement fusion targets, Nucl. Fusion **17**, 223 (1977).

[7] J. D. Lindl, R. L. McCrary, and E. M. Campbell, Progress towards ignition and burn propagation in Inertial Confinement, Phys. Today **45**(9), 32 (1992).

[8] J. Sanz, Self-Consistent Analytical Model of the Rayleigh-Taylor Instability in Inertial Confinement Fusion, Phys. Rev. Lett. **73**, 2700 (1994).

[9] A. R. Piriz, Hydrodynamic instability of ablation fronts in inertial confinement fusion, Phys. Plasmas **8**, 997 (2001).

[10] R. Betti, V. N. Goncharov, R. L. McCrory, and C. P. Verdon, Growth rates of the ablative Rayleigh-Taylor instability in inertial confinement fusion, Phys. Plasmas **5**, 1446 (2002).

[11] S. Atzeni and J. Meyer-ter Vehn, *The Physics of Inertial Fusion: BeamPlasma Interaction, Hydrodynamics, Hot Dense Matter* (Oxford University Press Inc., New York, 2004).

[12] J. C. Beale and R. D. Reitz, Modeling spray atomization with the Kelvin-Helmholtz/Rayleigh-Taylor hybrid model, Atomization and Sprays **9**, 623 (1999).

[13] C. Clanet and G. Searby, First Experimental Study of the Darrieus-Landau Instability, Phys. Rev. Lett. **80**, 3867 (1998).

[14] S. Zaleski and P. Julien, Numerical simulation of Rayleigh-Taylor instability for single and multiple salt diapirs, Tectonophysics **206**, 55 (1992).

[15] Z. G. Ji, *Hydrodynamics and Water Quality: Modeling Rivers, Lakes, and Estuaries*, 1st ed. (Wiley-Interscience, Hoboken, New Jersey, 2008).

[16] J. R. Garratt, Review: The atmospheric boundary layer, Earth-Science Reviews **37**, 89 (1994).

[17] D. D. Gray and A. Giorgini, The validity of the Boussinesq approximation for liquids and gases, Int. J. Heat Mass Transf. **19**, 545 (1976).

[18] D. H. Sharp, An overview of Rayleigh-Taylor instability, Physica D **12**, 3 (1984).

[19] J. R. Ristorcelli and T. T. Clark, Rayleigh-Taylor turbulence: Self-similar analysis and direct numerical simulations, J. Fluid Mech. **507**, 213 (2004).

[20] K. Read, Experimental investigation of turbulent mixing by Rayleigh-Taylor instability, Physica D **12**, 45 (1984).

[21] D. L. Youngs, Numerical simulation of turbulent mixing by Rayleigh-Taylor instability, Physica D **12**, 32 (1984).

[22] N. N. Anuchina, Y. Kucherenko, V. E. Neuvazhaev, V. N. Ogibina, L. I. Shibarshov, and V. G. Yakovlev, Turbulent mixing at an accelerating interface between liquids of different density, Fluid Dyn. **13**, 916 (1978).

[23] A. W. Cook and P. E. Dimotakis, Transition stages of Rayleigh-Taylor instability between miscible fluids, J. Fluid Mech. **443**, 69 (2001).

[24] M. J. Andrews and D. B. Spalding, A simple experiment to investigate two-dimensional mixing by Rayleigh-Taylor instability, Phys. Fluids A **2**, 922 (1990).

[25] P. F. Linden, J. M. Redondo, and D. L. Youngs, Molecular mixing in Rayleigh-Taylor instability, J. Fluid Mech. **265**, 97 (1994).

[26] G. Dimonte and M. Schneider, Density ratio dependence of Rayleigh-Taylor mixing for sustained and impulsive acceleration histories, Phys. Fluids **12**, 304 (2000).

[27] A. Banerjee and M. J. Andrews, Statistically steady measurements of Rayleigh-Taylor mixing in a gas channel, Phys. Fluids **18**, 035107 (2006).

[28] D. H. Olson and J. W. Jacobs, Experimental study of Rayleigh-Taylor instability with a complex initial perturbation, Phys. Fluids **21**, 034103 (2009).

[29] D. L. Youngs, Three-dimensional numerical simulation of turbulent mixing by Rayleigh-Taylor instability, Phys. Fluids A: Fluid Dynamics **3**, 1312 (1991).

[30] A. W. Cook, W. H. Cabot, and P. L. Miller, The mixing transition in Rayleigh-Taylor instability, J. Fluid Mech. **511**, 333 (2004).

[31] D. Livescu, J. R. Ristorcelli, R. A. Gore, S. H. Dean, W. H. Cabot, and A. W. Cook, High-Reynolds number Rayleigh-Taylor turbulence, Journal of Turbulence **10**, N13 (2009).

[32] G. Dimonte, D. L. Youngs, A. Dimits, S. Weber, M. Marinak, S. Wunsch, C. Garasi, A. Robinson, M. J. Andrews, P. Ramaprabhu, A. C. Calder, B. Fryxell, J. Biello, L. Dursi, P. MacNeice, K. Olson, P. Ricker, R. Rosner, F. Timmes, H. Tufo *et al.*, A comparative study of the turbulent Rayleigh-Taylor instability using high-resolution three-dimensional numerical simulations: The Alpha-Group collaboration, Phys. Fluids **16**, 1668 (2004).

[33] A. Banerjee and M. J. Andrews, 3D Simulations to investigate initial condition effects on the growth of Rayleigh-Taylor mixing, Int. J. Heat Mass Transf. **52**, 3906 (2009).

[34] B. Akula and D. Ranjan, Dynamics of buoyancy-driven flows at moderately high Atwood numbers, J. Fluid Mech. **795**, 313 (2016).

[35] P. E. Dimotakis, Turbulent Mixing, Annu. Rev. Fluid Mech. **37**, 329 (2005).

[36] Y. Kucherenko, A. Pylaev, V. Murzakov, A. Belomestnih, V. Popov, and A. Tyaktev, Experimental study into the Rayleigh-Taylor turbulent mixing zone heterogeneous structure, Laser Part. Beams **21**, 375 (2003).

[37] M. S. Roberts and J. W. Jacobs, The effects of forced small-wavelength, finite-bandwidth initial perturbations and miscibility on the turbulent Rayleigh-Taylor instability, J. Fluid Mech. **787**, 50 (2015).

[38] P. F. Linden and J. M. Redondo, Molecular mixing in Rayleigh-Taylor instability. Part I: Global mixing, Phys. Fluids A **3**, 1269 (1991).

[39] D. M. Snider and M. J. Andrews, Rayleigh-Taylor and shear driven mixing with an unstable thermal stratification, Phys. Fluids **6**, 3324 (1994).

[40] G. I. Taylor, Statistical theory of turbulence, Proc. R. Soc. A **151**, 421 (1935).

[41] A. L. Kistler and T. Vrebalovich, Grid turbulence at large Reynolds numbers, J. Fluid Mech. **26**, 37 (1966).

[42] P. Wilson, M. J. Andrews, and F. Harlow, Spectral nonequilibrium in a turbulent mixing layer, Phys. Fluids **11**, 2425 (1999).

[43] P. N. Wilson and M. J. Andrews, Spectral measurements of Rayleigh-Taylor mixing at small Atwood number, Phys. Fluids **14**, 938 (2002).

[44] P. Ramaprabhu and M. J. Andrews, Simultaneous measurements of velocity and density in buoyancy-driven mixing, Exp. Fluids **34**, 98 (2003).

[45] P. Ramaprabhu and M. J. Andrews, Experimental investigation of Rayleigh-Taylor mixing at small Atwood numbers, J. Fluid Mech. **502**, 233 (2004).

[46] N. J. Mueschke, M. J. Andrews, and O. Schilling, Experimental characterization of initial conditions and spatio-temporal evolution of a small-Atwood-number Rayleigh-Taylor mixing layer, J. Fluid Mech. **567**, 27 (2006).

[47] N. J. Mueschke, O. Schilling, D. L. Youngs, and M. J. Andrews, Measurements of molecular mixing in a high-Schmidt-number Rayleigh-Taylor mixing layer, J. Fluid Mech. **632**, 17 (2009).

[48] W. N. Kraft, A. Banerjee, and M. J. Andrews, On hot-wire diagnostics in Rayleigh-Taylor mixing layers, Exp. Fluids **47**, 49 (2009).

[49] A. Banerjee, W. N. Kraft, and M. J. Andrews, Detailed measurements of a statistically steady Rayleigh-Taylor mixing layer from small to high Atwood numbers, J. Fluid Mech. **659**, 127 (2010).

[50] A. Banerjee, Rayleigh-taylor instability: a status review of experimental designs and measurement diagnostics, J. Fluids Eng. **142**, 120801 (2020).

[51] O. Schilling, Progress on Understanding Rayleigh-Taylor Flow and Mixing Using Synergy Between Simulation, Modeling, and Experiment, J. Fluids Eng. **142**, 120802 (2020).

[52] B. Akula, M. J. Andrews, and D. Ranjan, Effect of shear on Rayleigh-Taylor mixing at small Atwood number, Phys. Rev. E **87**, 033013 (2013).

[53] B. Akula, P. Suchandra, M. M. Mikhaeil, and D. Ranjan, Dynamics of unstably stratified free shear flows: An experimental investigation of coupled Kelvin-Helmholtz and Rayleigh-Taylor instability, J. Fluid Mech. **816**, 619 (2017).

[54] M. Mikhaeil, Simultaneous velocity and density measurements of fully-developed Rayleigh-Taylor turbulent mixing, Ph.D. thesis, Georgia Institute of Technology, 2019.

[55] A. Banerjee, R. A. Gore, and M. J. Andrews, Development and validation of a turbulent-mix model for variable-density and compressible flows, Phys. Rev. E **82**, 046309 (2010).

[56] S. B. Pope, *Turbulent Flows* (Institute of Physics, University of Reading, Berkshire, 2000).

[57] A. Melling, Tracer particles and seeding for particle image velocimetry, Meas. Sci. Technol. **8**, 1406 (1997).

[58] I. Grant, Particle image velocimetry: A review, Proceedings of the Institution of Mechanical Engineers, Part C: J. Mech. Eng. Sci. **211**, 55 (1997).

[59] C. R. Wilke, A viscosity equation for gas mixtures, J. Chem. Phys. **18**, 517 (1950).

[60] D. Livescu, J. R. Ristorcelli, M. R. Petersen, and R. A. Gore, New phenomena in variable-density Rayleigh-Taylor turbulence, Phys. Scr. T **142**, 014015 (2010).

[61] A. Sciacchitano and B. Wieneke, PIV uncertainty propagation, Measurement Sci. Tech. **27**, 084006 (2016).

[62] V. N. Goncharov, Analytical Model of Nonlinear, Single-Mode, Classical Rayleigh-Taylor Instability at Arbitrary Atwood Numbers, Phys. Rev. Lett. **88**, 134502 (2002).

[63] A. N. Kolmogorov, The local structure of turbulence in incompressible viscous fluid for very large Reynolds numbers, Proc. USSR Acad. Sci. **30**, 299 (1941).

[64] D. Besnard, F. H. Harlow, R. M. Rauenzahn, and C. Zemach, Turbulent transport equations for variable-density turbulence and their relationship to two-field models, Technical Report No. LAUR-12303, Los Alamos National Laboratory, 1992 (unpublished).

[65] P. V. Danckwerts, The definition and measurement of some characteristics of mixtures, Appl. Sci. Res. Sec. A **3**, 279 (1952).

[66] C. D. Tomkins, B. J. Balakumar, G. Orlicz, K. P. Prestridge, and J. R. Ristorcelli, Evolution of the density self-correlation in developing Richtmyer-Meshkov turbulence, J. Fluid Mech. **735**, 288 (2013).

[67] D. L. Youngs, Numerical simulation of mixing by Rayleigh-Taylor and Richtmyer-Meshkov instabilities, Laser Part. Beams **12**, 725 (1994).

[68] T. Cebeci and A. M. O. Smith, *Analysis of Turbulent Boundary Layers*, 1st ed. (Academic Press Inc, New York, 1974).

[69] J. J. Charonko and K. Prestridge, Variable-density mixing in turbulent jets with coflow, J. Fluid Mech. **825**, 887 (2017).

[70] N. R. Panchapakesan and J. L. Lumley, Turbulence measurements in axisymmetric jets of air and helium. Part 1. Air jet, J. Fluid Mech. **246**, 197 (1993).

[71] N. R. Panchapakesan and J. L. Lumley, Turbulence Measurements in axisymmetric jets of air and helium. Part 2. Helium Jet, J. Fluid Mech. **246**, 225 (1993).

[72] J. L. Lumley, Computational modeling of turbulent flows, Adv. Appl. Mech. **18**, 123 (1979).